Using Profiles of Water Vapor Flux to Characterize Turbulence in the Convective Boundary Layer

by

KRISTY JANE WEBER

B.S., University of Maryland, 2014

A thesis submitted to the

Faculty of the Graduate School of the

University of Colorado in partial fulfillment

of the requirement for the degree of

Master of Arts

Department of Geography

2017

This thesis entitled:
Using Profiles Of Water Vapor Flux To Characterize Turbulence In The Covective Boundary Layer

written by Kristy Jane Weber
has been approved for the Department of Geography

_____
Peter Blanken

_____
Waleed Abdalati

_____
Tammy Weckwerth

Date_____

The final copy of this thesis has been examined by the signatories, and we find that both the content and the form meet acceptable presentation standards of scholarly work in the above mentioned discipline.

Weber, Kristy J. (M.A., Geography)

Using Profiles Of Water Vapor Flux to Characterize Turbulence in the Convective Bounday Layer

Thesis directed by Professor Peter D. Blanken

Abstract

The 2015 Plains Elevated Convection at Night (PECAN) field campaign sought to increase understanding of mechanisms for nocturnal severe weather in the Great Plains of the United States. A collection of instruments from this field campaign, including a water vapor Differential LiDAR (Light Detection Imaging And Ranging) (DIAL) and 449 MHz radar wind profiler were used to measure water vapor flux in regions between 300 m and the convective boundary layer. Methods to properly sample eddies using eddy-covariance were established, where analysis showed that a 90-minute Reynold's averaging period was optimal to sample most eddies. Additionally, a case study was used to demonstrate the additional atmospheric parameters which can be calculated from profiles of water vapor flux, such as the water vapor flux convergence/divergence. Flux footprints calculated at multiple heights within the convective boundary layer also show how a surface based instrument is sampling a completely different source than one taking measurements above 300 m. This result is important, as it shows how measurements above the surface layer will not be expected to match with those taken within a few meters of the surface, especially if average surface features such

as land use type and roughness length are significantly different. These calculated water vapor flux profile measurements provide a new tool to analyze boundary layer dynamics during the PECAN field campaign, and their relationships to PECAN's study areas such as mesoscale convective systems (MCSs), nocturnal low-level jets (NLLJs), elevated convective initiation, and the propagation of bores or wavelike features from nocturnal convective systems.

TABLE OF CONTENTS

CHAPTER

TABLES

Table

FIGURES

Figure

CHAPTER ONE

Research Objectives and Background

1.1 Introduction

This thesis seeks to analyze patterns of turbulence in regions that have previously been difficult to monitor, due to a lack of observational technologies. Previously, tall towers, which make measurements at heights typically 300 m (or more) above ground level (AGL), have been used to study turbulent fluxes in the lower portions of the boundary layer for extended periods of time, on the order of months to years (Baldocchi et al. 2001; Berger et al. 2001; Davis et al. 2003; Desai et al. 2015; Bakwin et al. 1998). Water vapor Raman Light Detection Imaging and Ranging (LiDARs), wind lidars, and Sonic Detection And Ranging (SODAR) have also been used to study profiles of turbulent fluxes via aircraft. However, aircraft measurements lack the ability to study long-term trends over an area, though these measurements do allow for patterns of turbulence to be studied in the upper portions of the boundary layer, and even above the entrainment layer (Desjardins et al. 1989; Kiemle et al. 2007, 1997; Ehret et al. 1999). Ground-based profiling systems, similar to those deployed on aircraft, have also been used to study turbulence. More recently, a water vapor DIfferental Absorption Doppler LiDAR system (DIAL) and 449 MHz radar wind profiler have been developed at the

National Center for Atmospheric Research (NCAR) to measure profiles of water vapor and turbulence, with a temporal frequency as high as 30 seconds. Both of these instruments have been compared to radiosondes profiles measured nearby with high correlation values, especially in the lower range gates measured by the instruments (300 m) (Weckwerth et al. 2016; Spuler et al. 2015; Lindseth et al. 2014, 2012b,a). This study aims to combine the DIAL and wind profiler observations for the first time in an effort to obtain water vapor flux profiles.

Both the DIAL and radar wind profiler were deployed at a site near Ellis, KS during the Plains Elevated Convection At Night (PECAN) field campaign in 2015.This six-week field campaign, from June 1st-July 15th 2015, sought to study mechanisms of nocturnal convection in four separate, yet related, research areas: convective initiation, Nocturnal Low-Level Jets (NLLJs), mesoscale convective systems, and bores. For this field campaign, a combination fixed and mobile instruments were deployed in order to monitor the growth and evolution of nocturnal convective systems, as well as properties of boundary layers during the late evening transition period, and NLLJs. Fixed Site #3 (FP3), was comprised of two smaller sites located within 2 km of each other, as shown in Fig. 1.1. The National Center for Atmospheric Research's (NCAR) site, located in a rural area just north of I-70 in Ellis, KS, had a co-located water vapor DIAL, 449 MHz radar wind profiler and Atmospheric Emmitance Radiance Interferometer (AERI), in addition to a meteorological station. Millersville University's (MU) site had an 8.5-m-tall flux tower, meteorological station, and radiosonde launching facility, and was

located west of the town of Ellis, right outside of a baseball field. By locating these two sites with very different measurement capabilities nearby each other, it was intended that observations between these two sites would complement each other. As a result, part of this analysis compares the sources of water vapor measured by both of these sites, in order to determine if the prevalent conditions allowed comparisons to be made between the profilers at the NCAR site, and the surface based instruments at the MU site. Later, this analysis will also look at profiles of latent heat flux, calculated using water vapor flux from the DIAL and radar wind profiler, and temperature profiles from the AERI.

1.2 Research Questions

The main questions that this thesis seeks to answer are:

(1) What is the optimal averaging period used to sample eddies above 300 m in the convective boundary layer?

(2) How does eddy size change with height?

(3) Using the flux footprint, can surface and elevated measurements of water vapor flux be compared?

(4) How can water vapor flux divergence be used to gain more insight into the movement of water vapor in a column through the day?

Each of these questions posed by this thesis are thoroughly discussed and used to gain more insight into how turbulence behaves within the convective boundary layer above 300 m. Answering these questions also aims to further the knowledge gathered in the PECAN field campaign by providing new tools to study patterns of

turbulence and water vapor flux during the late afternoon and evening, before nocturnal severe weather features and low-level jets form.

1.3 Site Details

1.3.1 Topography

The location of the flux tower is east of Ellis, KS, and directly north and west of a creek which is bordered by woody wetlands. The areas immediately outside of Ellis are used for farming, as well as for cattle ranching over large pastures (Fig. 1.1). Surface information, such as crop and land cover type was derived from the USDA's Crop Data Layer (CDL), and was used to produce a raster image of roughness lengths for momentum for the entire study area (Fig. 1.2). These roughness lengths were estimated from those given in Wieringa (1992), and are

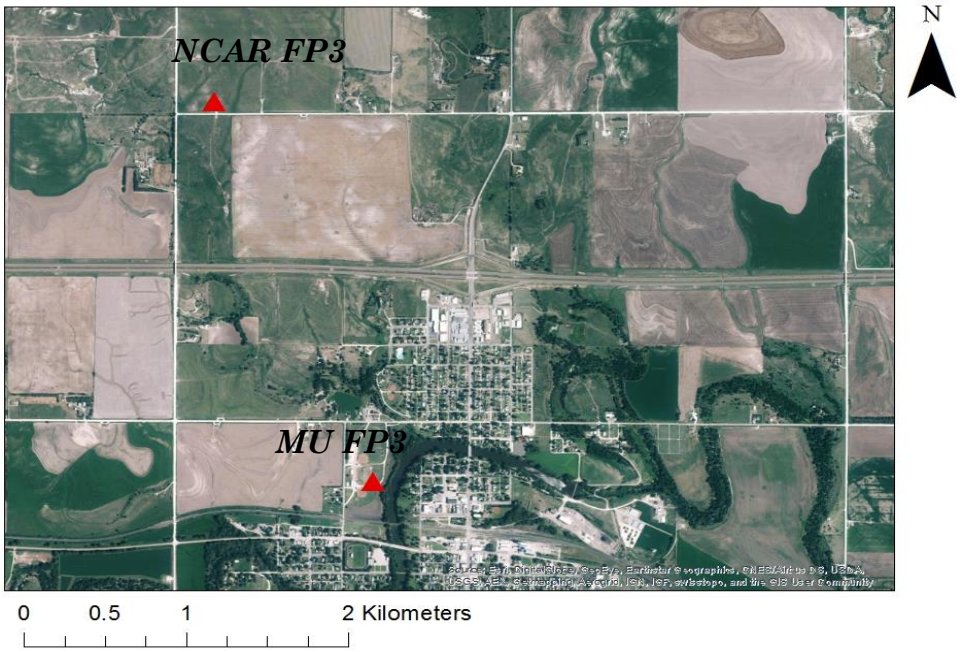

Figure 1.1. Landsat 8 image of Ellis, KS, showing proximity of MU and NCAR FP3 sites.

listed in Table 1.1. The crop data layer is based off of a decision tree classification using imagery from Landsat 8 and the Disaster Monitoring Constellation satellites (USDA 2015). This roughness length image allowed for visualization of the effect on different cover types on surface friction, and their effect on flux footprint shapes and extents. The MU FP3 site was located approximately 2.1 km southeast of the NCAR FP3 site.

Table 1.1. Typical roughness length values observed in areas surrounding Ellis, KS (Wieringa, 1992).

Surface Type	**Roughness Length (m)**
water	~0.0002
short grass	0.008-0.03
short ag. crops	0.04-0.09
mature wheat	0.12-0.18
bush/shrubs	0.35-0.45
trees	0.8-1.6
dense low buildings	0.4-0.7

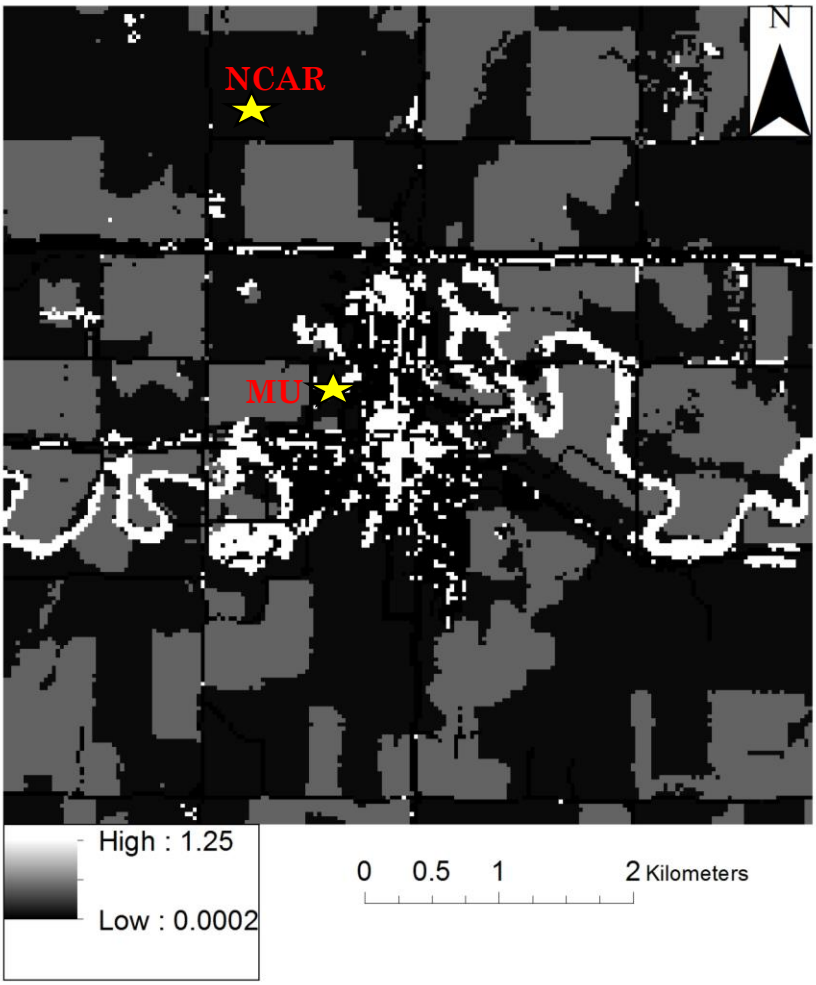

Figure 1.2. Roughness length values, in m, for areas surrounding NCAR and MU FP3 sites.

1.3.2 Weather at Ellis, KS During PECAN Field Campaign

For the entire duration of the PECAN field campaign, a total of 19.81 mm of rain were measured by the Vaisala weather station at the NCAR site in Ellis, KS, which is a difference of 62.49 mm from the climatological mean for this time period (NOAA NWS). Overall, Ellis, KS experienced much drier than usual conditions during the PECAN 2015 field campaign. Average surface meteorological parameters

for the entire duration of the PECAN field campaign are further summarized in Table 1.2.

Table 1.2. Summary of average surface meteorological parameters, provided by the Vaisala weather station at the NCAR FP3 site.

Temperature	**Surface Pressure**	**Water vapor density, ρ**	**Obhukov Length, L**	**Wind Speed**	**Wind Direction**
25.05 °C	1006.9 mb	13.12 g m^{-3}	0.64 m	4.73 m s^{-1}	156.67°

Water vapor, measured by the water vapor DIAL and the collocated Vaisala weather station are shown in Fig. 1.3. This water vapor composite took the average value for water vapor density, q, for each hour in the day and each altitude

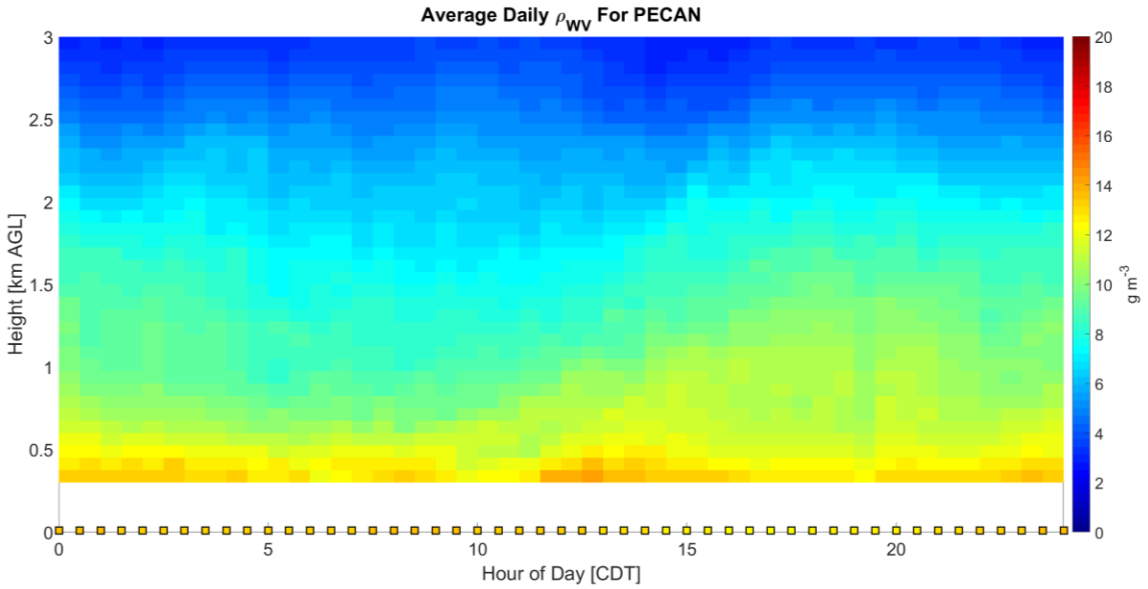

Figure 1.3. Composite water vapor averaged over entire PECAN study period. Profiles were calculated using the water vapor DIAL, while squares on the bottom are from the Vaisala weather station.

measured to show the average pattern of water vapor seen for the entire field campaign. It is particularly interesting to note the increase of water vapor at higher altitudes during the late afternoon due to buoyant eddies penetrating into a deepening boundary layer.

Similarly, Fig 1.4 shows the average vertical wind speed for the entire PECAN study period, averaged for each hour and altitude between the surface and 3 km, where measurements were available. Vertical wind data was provided by the sonic anemometer located at the 8.5 m level of the flux tower located at the MU FP3 site in Ellis, KS. Strong vertical motion can be seen in the afternoon hours, when convection is the strongest, while weak vertical motion and subsidence occurs at night.

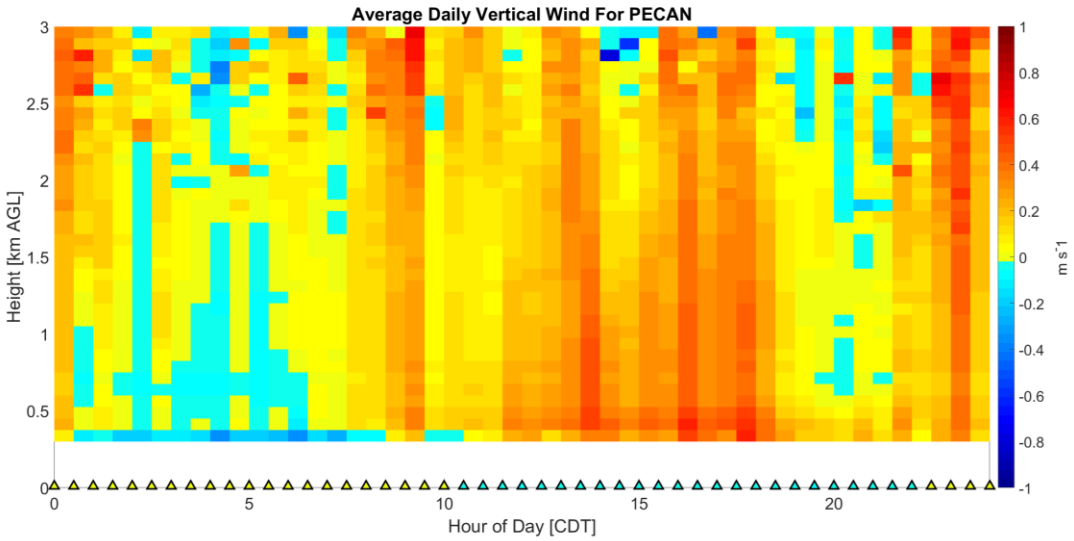

Figure 1.4. Composite vertical wind averaged over entire PECAN study period. Profiles were calculated using the 449 MHz radar wind profiler, while triangles on the bottom are from the MU flux tower.

1.4 Instruments

The instruments used in this analysis came the National Center for Atmospheric Research's (NCAR) Fixed Pisa 3 (FP3) site and Millersville University's (MU) Fixed Pisa 3 site. These sites were a part of a larger array of meteorological research sites deployed with fixed and mobile instruments during the PECAN 2015 field campaign.

1.4.1 NCAR FP3

1.4.1.1 Water Vapor Differential Absorption Lidar

NCAR's water vapor DIAL was developed over many iterations between NCAR and Montana State University. This laser-based profiler operates by transmitting two laser pulses located near an absorption line for water vapor, 828 nm. The online wavelength is tuned to be near the center of the water vapor absorption line 828.2000 nm, while the second, offline wavelength is centered on a line with little absorption due to water vapor, 828.2995 nm. The ratio of the return power of these two signals, along with the molecular cross section, are used to determine the range-resolved absolute humidity. This instrument operated during PECAN with a temporal sampling frequency of 30 seconds, and a spatial resolution of 75m. The lowest range gate of this instrument is 300 m due to the laser pulse length and overlap function, as the instrument cannot measure backscatter until the transmitted signal has completely left the transmitter. This causes the receivers of the DIAL to be temporarily "blinded", and unable to record data with the shortest return times, which are between the surface and 300 m above ground level (AGL) (Spuler et al. 2014, 2015; Weckwerth et al. 2016). In previous studies using

comparisons with radiosondes, measurements from the DIAL are accurate within 20% between 0.3-4.5 km at night, and 0.3 - 3.5 km during the day (Weckwerth et al. 2016).

1.4.1.2 449 MHz Radar Wind Profiler

The 449 MHz wind profiler uses multiple antennae to determine profiles of horizontal and vertical wind speed and direction. This wind profiler uses Bragg scattering to measure winds. Bragg scattering is caused by irregularities in temperature and humidity fluctuations in the atmosphere (Lindseth et al. 2012b, 2014). The spaced-antenna method is used to determine the horizontal velocity of wind. This method utilizes the multiple antenna receivers, instead of moving a single antenna, which allows for a greater temporal resolution as horizontal wind direction can be received simultaneously in operation, instead of losing time while the antenna is being repositioned (Briggs et al. 1950; Cohn et al. 1997; Ecklund et al. 1988). Wind velocity is determined using the spaced-antenna method by computing the cross-correlation between three or more different antenna receivers. The time lag between each of the receivers is then used to determine the horizontal velocity, and subsequently wind direction. The vertical wind speed is measured from the Doppler shift observed between the transmitted and received signal. For the PECAN 2015 field campaign, the radar wind profiler was operated in a 7-antenna hexagon, as can be seen in Fig.1.5. The vertical wind speeds used in this analysis were sampled every 75 m every 30 seconds, while the three-dimensional wind speeds and directions were sampled every 5 minutes with a spatial resolution

of 150 m. This instrument was configured to measure winds between 100 m and 5 km most accurately (Lindseth et al. 2012a).

Figure 1.5. 449 MHz radar wind profiler as set at NCAR FP3, June 2015

1.4.1.3 Atmospheric Emitted Radiance Interferometer

The Atmospheric Emitted Radiance Interferometer (AERI) is a passive profiling instrument that measures downwelling infrared radiance from 520 to 3000 cm^{-1}, at a resolution of approximately 1 cm^{-1}. This instrument is able to observe profiles of water vapor and temperature by inputting the observed radiances into a retrieval algorithm. This algorithm is based on the fact that channels of water vapor and temperature that are closer to the center of the absorption lines are more opaque at lower altitudes, while channels away from the center of the absorption line are more transparent, and can be used to induce information about the profiles

at higher altitudes. Additionally, local climatological data, as well as surface meteorological data, are used to produce more accurate profile retrievals (Turner and Löhnert 2014; Turner et al.; Wulfmeyer et al. 2015). Profile retrievals from this instrument were produced every 5 minutes. The vertical resolution varied logarithmically, with a resolution of ~50 m closest to the surface, and 1200 m at 2 km, with measurements becoming coarser with increased altitude.

1.4.1.4 Meteorological Station

A Vaisala WXT-520 was used to make surface observations of temperature, humidity, pressure, wind speed, and wind direction, and precipitation (Vaisala, 2012). Measurements from this station were recorded every 5 minutes. These variables were measured in order to compare surface meteorological parameters with those measured at higher altitudes by the profiling instruments (i.e., radar wind profiler, AERI, DIAL)

1.4.2 MU FP3

1.4.2.1 10 m Flux Tower

A 10-m-tall flux tower was deployed at the MU FP3 site. This tower included a number of instruments located at levels at 2 m and 8.5 m AGL. At the 2-m level, a Campbell Scientific CSAT-3 3D Sonic Anemometer, a Micromet Systems Q7.1 net radiometer, a Campbell Scientific HMP45C temperature and humidity sensor, a CR500 datalogger, and one Setra CS100 Barometric pressure transducer recorded observations. At the 8.5 m level, a second Campbell Scientific CSAT-3 3D Sonic Anemometer and a LI-COR LI-7500 Carbon Dioxide and Water Vapor sensor were

used to calculate flux measurements. These data were collected every minute for the case study used in this analysis.

1.5 Conclusions

In conclusion, the NCAR and MU FP3 sites during the PECAN field campaign were used to deploy a number of instruments to study atmospheric dynamics. Measurements made by the water vapor DIAL and radar wind profiler will be used in the subsequent chapters to establish a methodology for measuring water vapor flux in the convective boundary layer above 300 m. Additionally, these measurements will be used to demonstrate how water vapor flux can be used to study patterns in the convection boundary layer, as well as the movement of water vapor through the course of a day.

1.6 Chapter One References

Bakwin, P. S., P. P. Tans, D. F. Hurst, and C. Zhao, 1998: Measurements of carbon dioxide on very tall towers: results of the NOAA/CMDL program. Tellus B, **50**, 401–415.

Baldocchi, D., E. Falge, L. Gu, R. Olson, and others, 2001: FLUXNET: A new tool to study the temporal and spatial variability of ecosystem-scale carbon dioxide, water vapor, and energy flux densities. Bull. Am. Meteorol. Soc., **82**, 2415.

Berger, B. W., K. J. Davis, C. Yi, P. S. Bakwin, and C. L. Zhao, 2001: Long-term carbon dioxide fluxes from a very tall tower in a northern forest: flux measurement methodology. J. Atmos. Ocean. Technol., **18**, 529–542.

Briggs, B. H., G. J. Phillips, and D. H. Shinn, 1950: The analysis of observations on spaced receivers of the fading of radio signals. Proc. Phys. Soc. Sect. B, **63**, 106.

Cohn, S. A., C. L. Holloway, S. P. Oncley, R. J. Doviak, and R. J. Lataitis, 1997: Validation of a UHF spaced antenna wind profiler for high-resolution boundary layer observations. Radio Sci., **32**, 1279–1296.

Davis, K. J., P. S. Bakwin, C. Yi, B. W. Berger, C. Zhao, R. M. Teclaw, and J. G. Isebrands, 2003: The annual cycles of CO2 and H2O exchange over a northern mixed forest as observed from a very tall tower. Glob. Chang. Biol., **9**, 1278–1293.

Desai, A. R., and Coauthors, 2015: Landscape-level terrestrial methane flux observed from a very tall tower. Agric. For. Meteorol., **201**, 61–75.

Desjardins, R. L., J. I. MacPherson, P. H. Schuepp, and F. Karanja, 1989: An evaluation of aircraft flux measurements of CO2, water vapor and sensible heat. Boundary Layer Studies and Applications, Springer, 55–69.

Ecklund, W. L., D. A. Carter, and B. B. Balsley, 1988: A UHF wind profiler for the boundary layer: Brief description and initial results. J. Atmos. Ocean. Technol., **5**, 432–441.

Ehret, G., K. P. Hoinka, J. Stein, A. Fix, C. Kiemle, and G. Poberaj, 1999: Low stratospheric water vapor measured by an airborne DIAL. J. Geophys. Res. Atmos., **104**, 31351–31359.

Kiemle, C., G. Ehret, A. Giez, K. J. Davis, D. H. Lenschow, and S. P. Oncley, 1997: Estimation of boundary layer humidity fluxes and statistics from airborne differential absorption lidar (DIAL). J. Geophys. Res. Atmos., **102**, 29189–29203.

——, and Coauthors, 2007: Latent heat flux profiles from collocated airborne water vapor and wind lidars during IHOP_2002. J. Atmos. Ocean. Technol., **24**, 627–639.

Lindseth, B., W. O. J. Brown, J. Jordan, D. Law, T. Hock, S. A. Cohn, and Z. Popovic, 2012a: A New Portable 449-MHz Spaced Antenna Wind Profiler Radar. IEEE Trans. Geosci. Remote Sens., **50**, 3544–3553.

——, T. Kelly, W. O. J. Brown, T. Hock, S. A. Cohn, and Z. Popovic, 2012b: Low-cost 63% efficient 2.5-kW UHF power amplifier for a wind profiler radar. Microwave Symposium Digest (MTT), 2012 IEEE MTT-S International, 1–3.

——, W. O. J. Brown, T. Hock, S. A. Cohn, and Z. Popović, 2014: Wind profiler radar antenna sidelobe reduction. IEEE Trans. Antennas Propag., **62**, 56–63.

Spuler, S. M., K. S. Repasky, B. Morley, D. Moen, M. Hayman, and A. R. Nehrir, 2014: Field deployable diode-laser-based differential absorption lidar (DIAL) for profiling water vapor. Atmos. Meas. Tech. Discuss., **7**, 11265–11302.

——, ——, ——, ——, ——, and ——, 2015: Field-deployable diode-laser-based differential absorption lidar (DIAL) for profiling water vapor. Atmos. Meas. Tech., **8**, 1073–1087.

Turner, D. D., and U. Löhnert, 2014: Information content and uncertainties in thermodynamic profiles and liquid cloud properties retrieved from the ground-based Atmospheric Emitted Radiance Interferometer (AERI). J. Appl. Meteorol. Climatol., **53**, 752–771.

——, J. E. M. Goldsmith, and R. A. Ferrare, EJ Mlawer, and HE Revercomb, 2016: Water vapor observations in the ARM Program. Atmos. Radiat. Meas. Progr. First 20 Years, Meteor. Monogr,.

USDA, 2015: USDA National Agricultural Statistics Service Cropland Data Layer. Washington, D.C.,.

Weckwerth, T. M., K. J. Weber, D. D. Turner, and S. M. Spuler, 2016: Validation of a Water Vapor Micropulse Differential Absorption Lidar (DIAL). J. Atmos. Ocean. Technol., **33**, 2353–2372.

Wieringa, J., 1992: Updating the Davenport roughness classification. J. Wind Eng. Ind. Aerodyn., **41**, 357–368.

Wulfmeyer, V., and Coauthors, 2015: A review of the remote sensing of lower tropospheric thermodynamic profiles and its indispensable role for the understanding and the simulation of water and energy cycles. Rev. Geophys., **53**, 819–895.

2012: User's Guide: VAISALA Weather Transmitter WXT-520. Helsinki, 171 pp. http://www.vaisala.com/Vaisala Documents/User Guides and Quick Ref Guides/M210906EN-C.pdf.

CHAPTER TWO

Methods to Establish Flux Measurements Above 300 m

2.1 Introduction

The water vapor flux is a quantity that has been measured for decades at established tower sites throughout the world (Baldocchi et al. 2001; Berger et al. 2001; Davis et al. 2003; Desai et al. 2015; Bakwin et al. 1998). As a result, methodologies for defining corrections, proper flux averaging periods, and other considerations have been developed and tested many times for measurements made within the first 300 m of the surface. However, the region of atmosphere between the height of tall towers and the top of the convective boundary layer has yet to be studied as in-depth as surface-based flux tower measurements. This is because the ability to measure vertical profiles of wind and water vapor at a temporal frequency capable of performing eddy correlation flux calculations has only recently become more available. Many studies of water vapor flux profiles using Raman and differential lidars (Desjardins et al. 1989; Kiemle et al. 2007, 1997; Ehret et al. 1999) on aircraft have been performed, but these experiments lack the long-term data collections that flux towers obtain.

Ground-based profiling systems offer promise in this field, as the synergy of these profiling systems allow for this region within the boundary layer to be studied

for an extensive period of time, similarly to timescales which flux towers are able to operate and collect data. However, as a relatively new field, the methodologies used to study fluxes in this portion of the atmosphere need to be used carefully, as most calculations were developed to be used in portions of the atmosphere below what these profiling instruments can actually measure. Therefore, this chapter will take an in-depth analysis to study the feasibility of the equations developed to study fluxes in the lower atmosphere, as well as to determine parameters such as the Reynolds averaging period, for a number of heights between the lowest range gate of the profiling instruments, and the depth of the boundary layer.

2.2 Methods to Determine Flux Calculation

The purpose of this chapter is to establish methods to properly calculate turbulent fluxes from the DIAL and wind profiler, at heights greater than 300 m. The temporal averaging period for turbulent fluxes based on tower measurements within the surface layer has been well established in the range of 30-60 minutes, as these data have been available from long-term ecological study sites (Baldocchi et al. 2001; Aubinet et al. 2002). However, the lowest range gate measured by the water vapor DIAL was 300 m, which is above the highest measuring point of most flux towers. Research conducted with very tall towers has shown that averaging periods of one hour or greater are often needed higher measurement heights. These results were seen in a study using a tower with measurements made at 30 m, 122 m, and 396 m AGL, where measurements made at 122 m and 396 m AGL required at least an hour of averaging, which was verified using ogives (Berger et al. 2001;

Desjardins et al. 1989). The lowest level, at a height of 30 m AGL, required an averaging period of at least 30 minutes, which has been used through many sites with flux measured within 30 m of the surface (Baldocchi et al. 2001; Aubinet et al. 2002). A number of studies involving a combination of water vapor and wind profiling instruments, such as a water vapor DIAL/ Radio Detection and Ranging Radio Acoustic Sounding System (RADAR RASS) or water vapor DIAL/ Wind LiDAR combination have also required an increase in averaging period above the surface layer (Linné et al. 2007; Senff et al. 1994; Wulfmeyer 1999; Giez et al. 1999), with averaging times of 60 to 120 minutes quantified as necessary, rather than the standard 30 minutes typically used in the surface layer.

Because the PECAN field campaign used the WV DIAL and 449 MHz wind profiler over a time period of six weeks, many cases exist with different wind and stability regimes. The wealth of these data allows for a detailed analysis to be performed on multiple dates with similar stability and wind regimes over the same geographic location, allowing for the exclusion of dates with anomalous weather patterns. This was very important, as a number of dates within the field campaign exhibited optically thick clouds within the boundary layer, which the DIAL cannot see through, in addition to other conditions where the instruments could not accurately capture data.

2.2.1 Atmospheric Stability

Atmospheric stability was quantified by calculating the Obukhov length for each time a profile was measured by the WV DIAL and radar wind profiler. The Obukhov Length, L, is defined as follows by Stull, (1988):

$$L = \frac{-\overline{\theta_v} u_*^3}{kg\overline{(w'\theta_v')_s}} \qquad \text{Eq. 2.1}$$

In Eq. 2.1, $\overline{\theta_v}$ is defined as the mean virtual potential temperature, u_* is the surface frictio, k is the Von Kármán constant (assumed value of 0.4 used in this analysis), g is the acceleration due to gravity (constant at 9.81 m s^{-2}), and $\overline{(w'\theta_v')_s}$ is the surface virtual sensible heat flux. Because the lowest range gate of the water vapor DIAL and wind radar profiler is 300 m, a flux tower located 2.1 km south of the water vapor and wind profilers was used to calculate the Obukhov length. Positive values of L, indicating a negative sensible heat flux and subsidence, were used to study cases of stable environments. Negative values of L, indicating a positive sensible heat flux, were used to study cases of unstable, buoyant environments. Positive values for w indicate wind ascending away from the surface, while negative values for w indicate wind descending towards the surface.

2.2.2 Flux Averaging Period

The flux averaging period is of great importance, as the use of an improper averaging period T, when performing Reynolds averaging, can cause a significant increase or decrease in the measured flux values. If the averaging period is too short, the larger energy carrying eddies will only be partially captured, resulting in the total fluxes calculated to be much smaller than it should be, as well as a violation of first order turbulence closure approximations. Alternatively, if the

averaging period is too long, effects of the diurnal cycle will become present, causing an inaccurate value of flux to be calculated, due to the growth and decay of the boundary layer. For this reason, averaging periods between 15 and 180 minutes were tested in 15 minute increments. A limit of three hours was chosen because averaging for periods longer than this may include diurnal effects in the calculation of flux, which would be highly inaccurate. It would be expected that the optimal averaging period for flux averaging would be short near the surface, as eddies here are interacting with topography, introducing friction, and preventing the eddies from growing to a larger size. A similar effect would be found near the top of the convective boundary layer, as friction introduced by wind shear would be responsible for preventing eddies from reaching a larger size. Within the middle of the boundary layer, one would expect the turbulent eddies to be similar in size. Above the surface layer, one would expect turbulent eddies to increase to an optimal length, and remain this sze until the entrainment zone is reached. Here, eddy size would likely decrease again due to the destruction of eddies because of wind shear. For these reasons, it is very important to determine proper averaging periods as a function of z, where z is the height above the surface.

2.2.2.1 Ogive

The method of Ogives was employed in a manner similar to (Desjardins et al. 1989; Giez et al. 1999; Lee et al. 2006). An Ogive is calculated as the cumulative co-spectrum, taken from high to low frequencies. This method is able to measure the relative contribution of each frequency that makes up the entire Fourier spectrum

of the measured flux. As a result, the final Ogive will yield an asymptotic shape, where the asymptote symbolizes the portion of the spectrum where frequencies do not make a major contribution to the total flux. Ideally, the portion of the spectrum where this asymptote occurs will form at frequencies lower than the flux averaging frequency. If this is not the case, then a lower flux averaging frequency (longer averaging time) must be employed in order to capture the eddies carrying the most energy and mass. Ogives were calculated for a number of flux averaging periods, as well as day/night and unstable/stable cases for heights between 300 m and the top of the boundary layer.

2.2.2.2 Daily Means of Turbulent Fluxes

An alternative method to study the impact of Reynolds averaging on flux calculation is to calculate the mean flux over a specific time period for a variety of conditions. This method was adapted from an earlier study done by Blanken et al., (1998), in which a number of Reynolds averaging periods were compared to determine the proper averaging period above and below a forest canopy. The mean latent heat flux for a 12-hour period was normalized to the mean 30-minute latent heat flux in order to demonstrate how effectively flux was captured as the Reynolds averaging period was increased, from one to 30 minutes. Since the data being used for PECAN was captured at heights far above the canopy height ($z > 300$m), one would expect the averaging period to be longer than that observed within the surface layer. In this study, the mean latent heat flux at a particular altitude and

averaging period was normalized to the maximum latent heat flux at that altitude. This was done to highlight the frequencies in which the most flux is captured.

For this analysis, a 5-hour period was chosen to study water vapor flux, from 11-16 Central Daylight Time (CDT = UTC – 5 hr) for daytime flux on July 5th, and 23-04 CDT for nighttime flux on the night of July 4th-5th. A 5-hour period was chosen as it was the longest time in which a continuous spectrum could be calculated, as missing data due to optically thick clouds would otherwise cause discontinuities in the data. The actual time period was chosen since this was when solar heating of the surface was the strongest, leading to the production of eddies in an unstable atmosphere. For nighttime, this time period was used as it covered a time when solar radiation had ceased to occur for at least 2 hours, therefore the influence of surface heating on the production of eddies was minimal.

2.2.5 Coordinate Rotation of the Wind Field

In order to account for the effect of terrain and instrument placement, wind data are transformed from a Cartesian to streamline-based coordinate system. The planar-fit method (Wilczak et al. 2001) was used to apply this transformation, as the average u and v wind components were only available every 5 minutes. The w component sampled every 30 seconds. This discrepancy in averaging periods is caused by different methods used to calculate horizontal and vertical components of wind, as the methods to determine horizontal wind speeds and direction require a longer sampling period. The planar fit method uses three-dimensional wind data over a series of many data runs (the 5-min averaging periods) to determine a set of

statistical coefficients, b_0, b_1, and b_2, which are then used to rotate the u, v, and w wind vectors for each data run. The final product is a set of wind vectors in which the deviations of the instantaneous v and w components from the 5-minute means are minimized, and the u component is in the direction of the wind streamline.

Rotating wind vectors to a stream-wise coordinate system is extremely important for calculating fluxes as even slightly sloping terrain can cause the vertical wind component to be contaminated with erroneously high wind velocity magnitudes (Deacon and Kraus 1968; Kaimal and Haugen 1969; Dyer 1981). However, this effect is expected to decrease as altitude increases, due to the wind flow decoupling from surface friction and sloping effects. This analysis will see the effect of wind coordinate transformation as a function of altitude by studying how the coefficients solved for in the planar fit algorithm change with height.

2.2.6 Water Vapor Flux Calculation

The flux itself represents a pattern in which two variables of interest co-vary as a function of time. For this analysis, the covariance of the vertical wind speed with water vapor density was used. Looking at how these patterns vary as a function of height and stability can reveal a lot about the evolving thermodynamic situation in the atmosphere, as well as provide insight to whether or not convective initiation will occur (Wulfmeyer et al. 2016). During times of strong atmospheric stability, such as an overcast day, or nighttime, one would expect the water vapor flux profile near the surface to be very small, and close to zero. This is because at night, when conditions are more stable, much smaller wind movements will inhibit the large-

scale movement of moisture that is seen during more convective daytime conditions. Subsidence will occur as the surface cools, allowing for air to descend as well as dry adiabatically as it descends, yielding very small, positive water vapor fluxes. As turbulence becomes more suppressed during more stable conditions, some calculations of water vapor flux may be positive or negative, but very close to zero due to the vertical movement of air becoming more sporadic under conditions with little to no turbulence.

During unstable conditions, such as when daytime clear skies or small to medium cumulus clouds are present, a positive water vapor flux would be expected near the surface. This is because the solar radiation heating the surface will cause thermals to be produced, which will rise given sufficiently buoyant conditions and an unstable environmental lapse rate. This movement will cause an upward movement of air, which will also bring moisture evaporated from the soil and vegetation upwards with the parcel of air. Since the parcel of air will cool and perhaps condense as it rises, with multiple buoyant eddies contributing more moisture, the moisture within the convective boundary layer will increase. Therefore, the positive, upward movement of the wind, and positive (moistening) of the lower atmosphere will yield a positive water vapor flux. As the parcel of air rises higher in the atmosphere, the magnitude of water vapor flux will decrease but remain positive until one of two things happens: (1) the water vapor condenses into liquid form, or (2) the top of the boundary layer is reached. In the first situation, water vapor flux will become negative as the amount of water in the gaseous state

will decrease as it is condensed into the cloud. For the second situation, the combination of dry air being entrained, as well as the deepening of the boundary layer in the late afternoon will cause the upper regions of the mixed layer to become drier as air moves upwards, yielding a negative water vapor flux.

Because the vertical profile of water vapor flux changes as a function of stability, the analysis in this study will focus on how stability, as well as height, contribute to the observation of water vapor flux. In addition, it is expected for other observations, such as mean eddy size, and Reynolds averaging period, to change as a function of height and stability. This comprehensive analysis will employ a number of analytical techniques in order to quantitatively determine the proper Reynolds averaging period, which will then lead to the calculation of the mean eddy size, and average magnitude of water vapor flux as a function of height.

The water vapor flux was calculated using water vapor profiles derived from the National Center for Atmospheric Research's (NCAR) Water Vapor Differential Absorption Lidar (DIAL). Information specifying the engineering aspects of this instrument can be found in Spuler et al. (2015). Wind data used to calculate water vapor flux were derived from NCAR's 449 MHz Modular Radar Wind Profiler (Lindseth et al. 2012a,b, 2014). This analysis used data from these instruments with a temporal resolution of 30 seconds, and a vertical spatial resolution of 75 m. For PECAN, the laser pulse length of the water vapor DIAL was configured so that the lowest usable range gate was 300 m. Because the wind profiling radar uses backscatter to calculate wind from radar returns, wind is often difficult to detect

when the air is clean and clear of particles to provide backscatter informatio. For this reason, much of the data used to calculate water vapor flux lies in vertical profiles between 300 m and the top of the boundary layer (1.5-2.1 km). Taylor's frozen turbulence hypothesis was satisfied by removing any time period when the turbulent intensity (standard deviation) of the stream-wise wind was greater than twice the value of the stream-wise mean wind velocity (Taylor 1938; Willis and Deardorff 1976).

Data derived from the water vapor DIAL yields profiles of water vapor molecular number density, in units of molecules cm^{-3}. In order to calculate water vapor flux in more intuitive units, the molecular number density was converted to water vapor density, in units of g m^{-3}, as seen in Eq. 2.2 :

$$\rho_{H_2O} = \left(\frac{ND \times MM_{H_2O}}{AN} \right) \times 10^6 \qquad \text{Eq. 2.2}$$

In this equation, *ND* represents the molecular number density (measured by water vapor DIAL), MM_{H2O} represents the molecular weight of water (18.01 g mol^{-1}), and *AN* represents Avogadro's Number (6.022×10^{23} mol^{-1}).

To calculate the flux, the instantaneous vertical wind is multiplied by the instantaneous scalar (water vapor density). This instantaneous flux is then averaged over the Reynolds averaging period to yield the eddy flux. Eq. 2.3 and 2.4 illustrate the calculation of the eddy flux using the number of points, *N*, in each Reynolds averaging period, *T* (Stull 1988).

$$\overline{w's'} = \frac{1}{N} \sum_{i=0}^{N-1} (w_i - \bar{w})(s_i - \bar{s}) \qquad \text{Eq. 2.3}$$

$$\overline{w's'} = \frac{1}{N}\sum_{i=0}^{N-1} w_i' s_i' \qquad \text{Eq. 2.4}$$

In Eq. 2.3 and 2.4, w_i indicates the instantaneous wind, $\bar{w}$ indicates the average wind for the Reynolds averaging period, and w_i' indicates the instantaneous deviation from the mean wind. Likewise, the same notation has been used for the scalar of choice, s. $\overline{w's'}$ represents the eddy-covariance flux of the scalar of interest. In this study, $\overline{w'q'}$ will be used to note the eddy covariance water vapor flux.

2.2.7 Convective Boundary-Layer Depth Estimation

The convective boundary layer depth, z_i is used as a scaling factor to study changes in turbulent eddy characteristics as a function of normalized height. In order to calculate this depth, a number of techniques were tested to optimally solve for this quantity. This included solving for the altitude at which the maximum gradient in backscatter, water vapor density, and wind occurred (Stull 1988), or the maximum in signal to noise ratio measured by the radar wind profiler (Angevine et al. 1994). The water vapor DIAL was used to study the relation of backscatter and water vapor density with convective boundary layer height, while the radar wind profiler was used to determine the convective boundary layer height from profiles of signal to noise ratio and horizontal and vertical wind speeds. However, the complex vertical profiles derived from the DIAL was often unable to solve for a reasonable boundary layer depth, as a result of multiple boundaries being present at times within a vertical profile, or missing data. Moisture contours were explored as a method to define the edge of the boundary layer. However, this method

oversimplifies the location of the top of the boundary layer, as the value of moisture chosen to define the edge of the boundary layer changes seasonally, as well as in the presence of strong mesoscale features. The contour method also fails to capture the depth of the entrainment layer. Using the maximum in the signal to noise ratio of the radar wind profiler was also unable to clearly and continuously define boundary layer heights. Eventually, it was decided that the boundary layer retrieval from the AERI instrument was the best method to study boundary layer evolution. This is because the boundary layer depths are determined using the potential temperature profiles, which radiosonde BL depth estimations use, in addition to retrievals being available once every 5 minutes, as opposed to every couple of hours with radiosonde launches.

2.3 Results and Discussion

2.3.1 Atmospheric Stability

Atmospheric stability was analyzed for the entire duration of the PECAN field campaign. Fig. 2.1 shows the variability of for July 4th – 5th, with daytime values of L being negative, and nighttime values being positive. Stability values were averaged to an hour from minute data available from the MU flux tower. For daytime, the average value of L varied between -100 m to -200 m, and the nighttime values of L varied between a few meters up to 100 m. The average value of L for the entire field campaign was 10.23 m. These data show that daytime conditions for July 4th and 5th exhibited unstable conditions, while more stable conditions were observed at night. The unstable, daytime conditions allowed for buoyant thermals to

be produced and contribute to the growth of the convective boundary layer during the day. At night, the stable conditions inhibited vertical motion of eddies, thereby greatly reducing turbulence during this period.

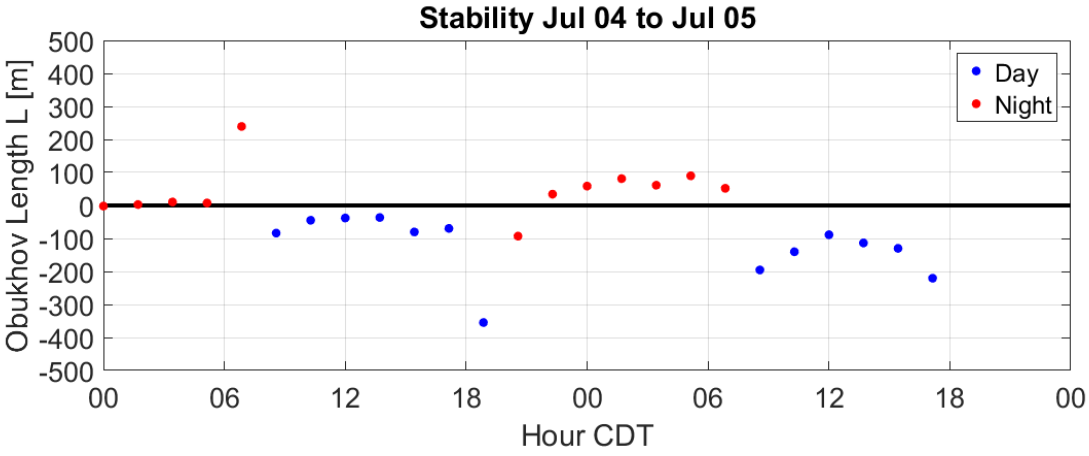

Figure 2.1. Obukhov Length calculated using data from the MU flux tower, and Eq. 2.1. Data is averaged hourly from 00 CDT July 4th through 24 CDT July 5th.

2.3.2 Flux Averaging Period

2.3.2.1 Ogive

Ogives were the first method used to analyze the effect of Reynolds averaging period on the daily accumulated flux. Data during unstable daytime conditions showed that an averaging period of 90 minutes was sufficient for most heights within the boundary layer, as seen in Fig. 2.2a. For this analysis, July 5th, 2015 was used as the test case to determine turbulence parameters. More than one day was examined to determine turbulence parameters, and many other days showed similar characteristics to this 24-hr period. However, this date had the clearest patterns, and was therefore chosen as the case to perform this analysis.

It was particularly interesting to see that for the Ogives calculated for the day, in Fig. 2.2a, nearly all of the ogives collapsed onto the same curve, with a peak at 90 minutes. This analysis therefore shows that 90 minutes was the optimal averaging period for daytime unstable turbulent conditions for all sampling heights. Another interesting feature in this plot is the undulation due to the addition of both positive and negative flux components, as opposed to the accumulation of only positive components, which would show the plot only increasing. This undulation captures how different averaging periods can be more effective at capturing the flux, as a Reynolds averaging period that is too short or too long will capture only part of an eddy. A Reynolds averaging period that most closely matches the period of the waves created by turbulence will therefore capture the most turbulence.

At night, when more stable conditions prevailed, the ogives in Fig 2.2b reveal that a Reynolds averaging period of 120 minutes was sufficient to capture the turbulent eddies. This longer averaging period could be due to weaker winds near the surface with similarly sized eddies taking longer to pass by the sensor. Though a number of nights during PECAN experienced strong winds near the surface due to the NLLJ, the night chosen for this analysis does not. Another characteristic to note is that at night, the radar wind profiler did not work as well. This is because the radar wind profiler relies on Bragg scattering in order to determine wind speeds. At night, when there is less mixing, the air above the surface is much “cleaner”, that is, the air contains much less moisture to create moisture and pressure graduents which would induce Bragg scattering returns. Turbulence at night times is also

more erratic, and may fail to develop the wave like components which are present during daytime convection. For this reasons, other tests, such as the spectrum of the data, should be assessed in order to determine the accuracy of the data.

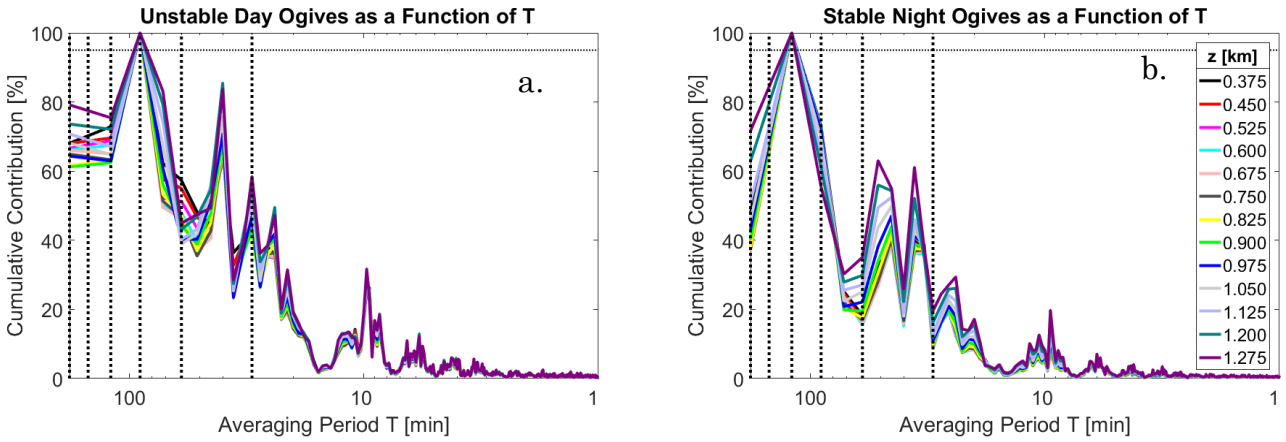

Figure 2.2. Ogives plotted as a function of boundary layer height. (a) indicates unstable conditions, while (b) indicates stable conditions. The horizontal black line indicates the 95% accumulated threshold, which is used to determine when a sufficient amount of flux has been accumulated. Vertical black lines are drawn every 30 minutes between 30 and 180 minutes.

2.3.2.2 Daily Mean of Fluxes

Determining the daily mean of fluxes was the second method used to study the influence of Reynolds averaging period on the calculation of flux.

For unstable daytime periods, a number of patterns were seen in the lowest range gates measured by the profiling instrument (Fig. 2.3a). From 300-500 m, a maximum was seen to occur around 165 minutes, while between 500-1000 m, maxima occurred for averaging periods less than 60 minutes. Between 1000-2000 m, the maxima again switch to periods longer than 120 minutes. The reason for the higher frequency maxima observed between 500-1000m is not clear, but one

possible reason could be because this region of the atmosphere experienced the most change in boundary layer structure during the daytime. In the morning, the boundary layer quickly grew into this region, before reaching its maximum around 1600 CDT, as seen in Fig. 2.6. Another interesting feature is that the boundary had the greatest variability between 15-17 CDT, which may have been due to the entrainment zone becoming deeper as well. Eddies entrained from the free atmosphere interacting with buoyantly generated eddies could have been the cause for the smaller eddies seen in this region, as the interaction between these different turbulence producing mechanisms, such as shear due to friction and buoyancy ,can be very hard to predict. However, this analysis provides insight into the possibility of eddies produced by different forces interacting with each other, and how this may interact with the calculation of flux measurements. As a result, a Reynold's averaging period of 90 minutes was chosen for calculating flux for this analysis. This is because of the Ogive analysis showing many different heights collapsing into a plot that agrees with this number, which shows a clear pattern of turbulence within the convective boundary layer. Fig. 2.3a is a bit more unclear, but average flux values with a 90-minute averaging period within the convective boundary layer were often within 70% of the maximum flux value. This shows that although this plot may highlight peaks at certain averaging periods, the difference in the flux calculated at these different averaging periods are not significantly large.

At night, with the decomposition of the convective boundary layer, patterns of turbulence become more complicated. In Fig. 2.3b, below 1000 m, some of the altitudes show multiple averaging periods where the average flux value calculated is very close to the maximum flux value. One reason for this could be due to less mechanisms being present at night for turbulent flux to occur. The buoyant flux is

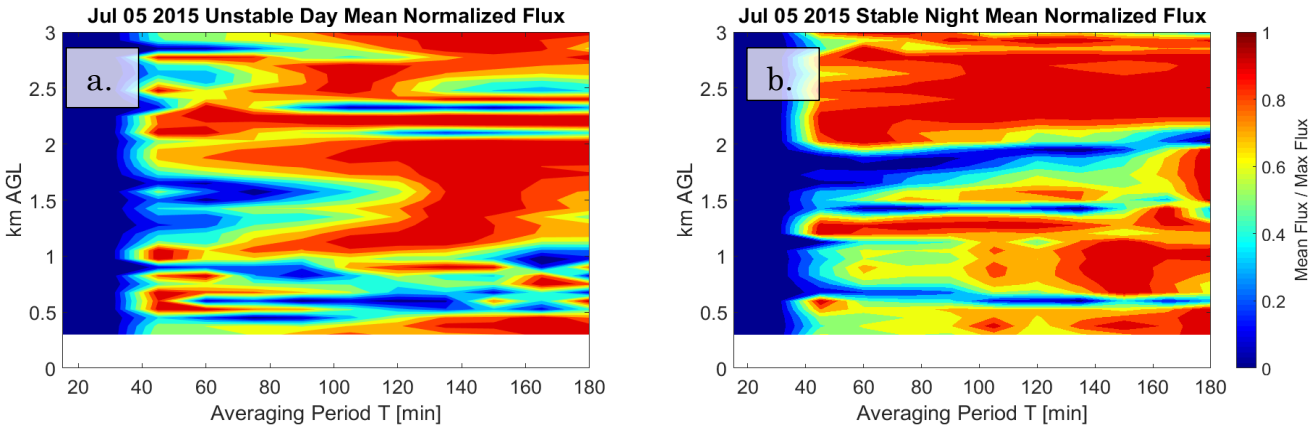

Figure 2.3. Mean flux normalized to maximum flux calculated at each altitude. Daytime mean z_i height was 1.31 km, with a maximum of 2.52 km.

reduced due to the absence of solar heating, and winds tend to be much weaker, reducing the number of turbulent eddies produced by surface friction. Therefore, any flux that does occur will not vary largely in magnitude between the different Reynold's averaging periods. Additionally, measurements at night may be far less accurate than during the day due to the aforementioned lack of Bragg scattering used by the radar wind profiler to make measurements. Therefore, this analysis shows that trying to estimate the Reynold's averaging period for nighttime measurements may not be possible with the current instrument setup. In the future, utilizing profilers with similar optical measurement methods, such as adding a wind lidar, would greatly reduce this error.

2.3.3 Results of Applying Water Vapor Flux Calculations

2.3.3.1 Topographic Rotation Correction for Three-Dimensional Winds

A rotation correction was applied to the wind data in order to align the vertical wind component orthogonally to the stream wise wind. This correction, based on the planar fit method (Wilczak et al. 2001) corrected winds in order to align the vertical winds to be orthogonal to a streamwise plane calculated as a result of topography. The rotation correction was calculated using wind data from June 2nd-July 15th, 2015. The effect of rotation was then studied as a function of flux averaging period and stability. The percent difference was calculated as follows:

$$\text{Percent Difference} = \left(\frac{\text{Flux}_{\text{rot}} - \text{Flux}_{\text{nonrot}}}{\frac{1}{2}(\text{Flux}_{\text{rot}} + \text{Flux}_{\text{nonrot}})} \right) \times 100 \qquad \text{Eq. 2.5}$$

This calculation was used to quantify the differences caused by the application of the rotation correction. In the denominator, the average of the rotated and non-rotated flux value was used because neither of these values were assumed to be the "correct" value. For this analysis, data from July 5th was used to produce Fig. 2.4. In Fig. 2.4a, the effect of rotation can be seen when applied to unstable daytime conditions. Within the first 1.5 km of the atmosphere, the percent difference was less than 10% for most averaging periods. However, between 60 and 105-minute averaging periods, differences greater than 50% were observed. These anomalously large differences could be due to the fact that this region saw the most rapid boundary layer growth in the afternoon and most rapid decay in the evening. However, it is interesting to note that these differences were not seen in other averaging periods which may have been due to under sampling eddies. Therefore,

these periods with large differences should not be completely discredited, as the Ogive and daily mean flux methods showed that these averaging periods captured eddies contributing to fluxes that would otherwise not be observed. Additionally, for this reason, it is best to use wind data that has been correctly rotated in order for the vertical flux to be properly calculated.

At night, greater atmospheric stability leads to conditions with lower wind speeds, often causing turbulence to become weak and intermittent. For this reason, the planar fit correction may not effectively capture the movement of turbulent eddies, as the movement of turbulent eddies at low to calm wind speeds may not follow topography as predicted. Rather, the sporadically produced eddies will have a more random movement, without the mean horizontal wind to produce the conditions necessary for stationarity to occur. In Fig. 2.4b, one can see the values of percent difference exceeding 50% for much of the heights and Reynolds averaging periods. Because these extreme differences were seen for most of the measurements during stable nighttime conditions, this may be seen as a demonstration of flux calculation becoming less dependable during low wind speed conditions. As a result, the planar fit coordinate rotation seems to be a necessary tool in order to represent more accurate fluxes, especially during daytime unstable conditions. The planar fit method was applied to nighttime data, since more error in the calculation of flux seems to be due to non-stationarity rather than over or underestimations of flux using the planar fit method. However, fluxes measured at night will be treated much more cautiously due to these calculations being more error prone.

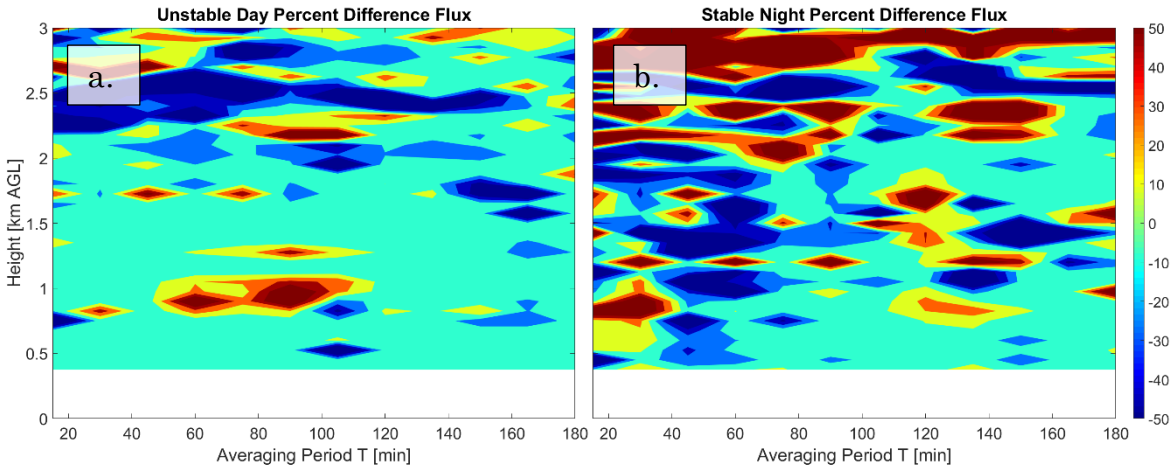

Figure 2.4. Percent difference as a function of averaging period T and height. Daytime mean z_i height was 1.31 km, with a maximum of 2.52 km.

Rotation as a function of height and Reynolds averaging period was also studied for the 6-week study period of PECAN (Fig. 2.5). This analysis was used to determine how topography affected streamlines of wind as a function of height. Rotation angle between the *x*-*z* and *y*-*z* planes seemed to change to most within the first 2 km of the atmosphere, as the *x*-*z* angles increased from nearly 0° to 0.5° (fig. 2.5a), and the *y*-*z* angles changed from 0.5° to 0° (Fig. 2.5b). Above 2 km, *x*-*z* rotation angles stabilized to a value closer to 1.5°, while *y*-*z* angles stabilized to values closer to -1°. Though these rotation angles are very small, the fact that they persist

throughout the first 5 km of the atmosphere suggests that a minor misalignment of the radar beam from the 449 MHz profiler may lead to significant measured tilts in the atmosphere that may not be related to topography. Overall, this analysis of rotation angles as a function of height shows that applying a coordinate rotation of data is not only important to remove topographic effects from data, but also to remove sensor alignment errors.

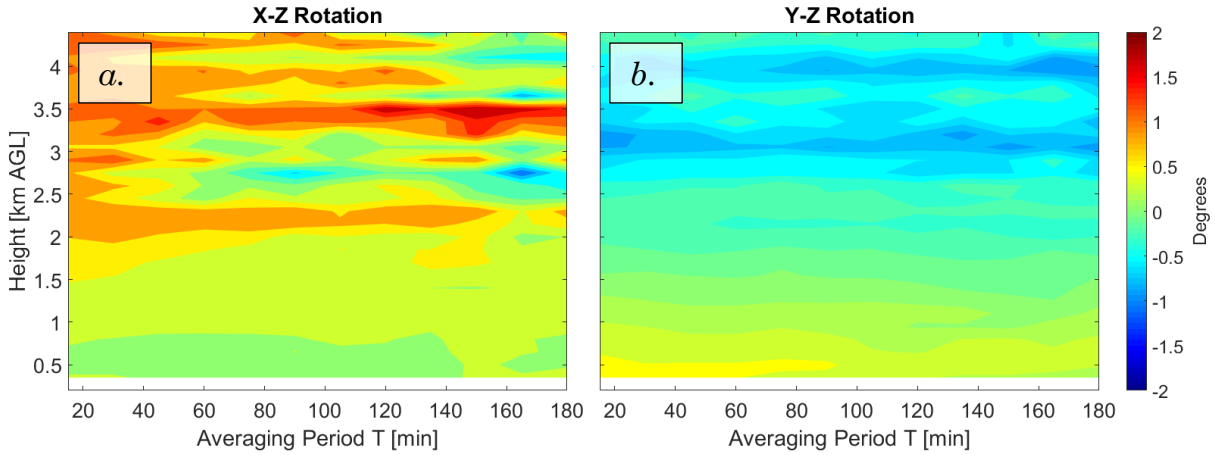

Figure 2.5. Rotation of *z*-axis from the *x* and *y* axis as a function of height and Reynolds averaging period. Daytime mean z_i height was 1.31 km, with a maximum of 2.52 km.

2.3.4 Water Vapor Flux Throughout July 5th

The water vapor flux was calculated at 90-min intervals for the entire field campaign of PECAN. A typical day with afternoon convection is shown in Fig. 2.6. The night of July 4th, day of July 5th, and transition to the evening of July 5th are shown in Fig. 2.6. One can see the lack of deep moist convection and the inability of the algorithm to calculate boundary layer height during the overnight hours. Then,

after 0900 CDT, boundary layer convection increases as the production of thermals cause moisture-laden eddies to penetrate deeper into the atmosphere, increasing the depth of the boundary layer into the late afternoon and early evening. In the DIAL water vapor imagery (Fig. 2.6a), one can also discern the formation of optically thick, liquid water loaded clouds above 2.5 km after 1200 CDT. This is due to the transport of moist eddies from the surface to the top of the boundary layer. Higher variability in boundary layer height seen between 1500-1700 CDT is an indication of a deepening entrainment zone as the boundary layer reaches its maximum height and the greatest amount of convection occurs.

The growth of the convective boundary layer can also be seen in the vertical wind data in Fig. 2.6b. Vertical wind speeds are weak and more negative overnight from 0200 – 0600 CDT, indicating subsidence. After about 1100 CDT, boundary layer convection is seen in the form of vertical wind speeds increasing as well as exhibiting sinking and rising motions, as indicated by higher magnitude wind rising upwards and lower magnitude wind moving towards the surface. As solar radiation warms the surface, causing thermals to form, the overall motion of vertical wind speed during the day is upwards, with a few pockets of sinking air interspersed between these thermals.

Convection can also be seen in Fig 2.6c, as the instantaneous water vapor flux changes in magnitude over time. Starting at 2100 CDT on July 4th, the magnitudes of the flux are seen to decrease and approach 0. This is because of the decrease in turbulence that occurs overnight. When solar radiation is no longer able

to produce thermals at the surface, after sunset around 2000 CDT, turbulent eddy production becomes greatly inhibited and eventually ceases. A few occurrences of very negative and very positive water vapor flux are seen overnight, between 0400 - 0700 CDT on July 5th, but this may be due to flux calculations in this portion of the atmosphere being more erroneous under more sporadic turbulence conditions. After 0900 CDT, when solar radiation produces thermals at the surface, the magnitude of the flux is seen to increase with moist air rising to the top of the boundary layer. Moist, buoyant thermals will continue to deepen the boundary layer by punching through the top of the entrainment layer, with further deepening occurring in the late afternoon. The data shown in Fig. 2.6c also become much "noisier" after 1100 CDT as many turbulent eddies become difficult to discern from each other. Another

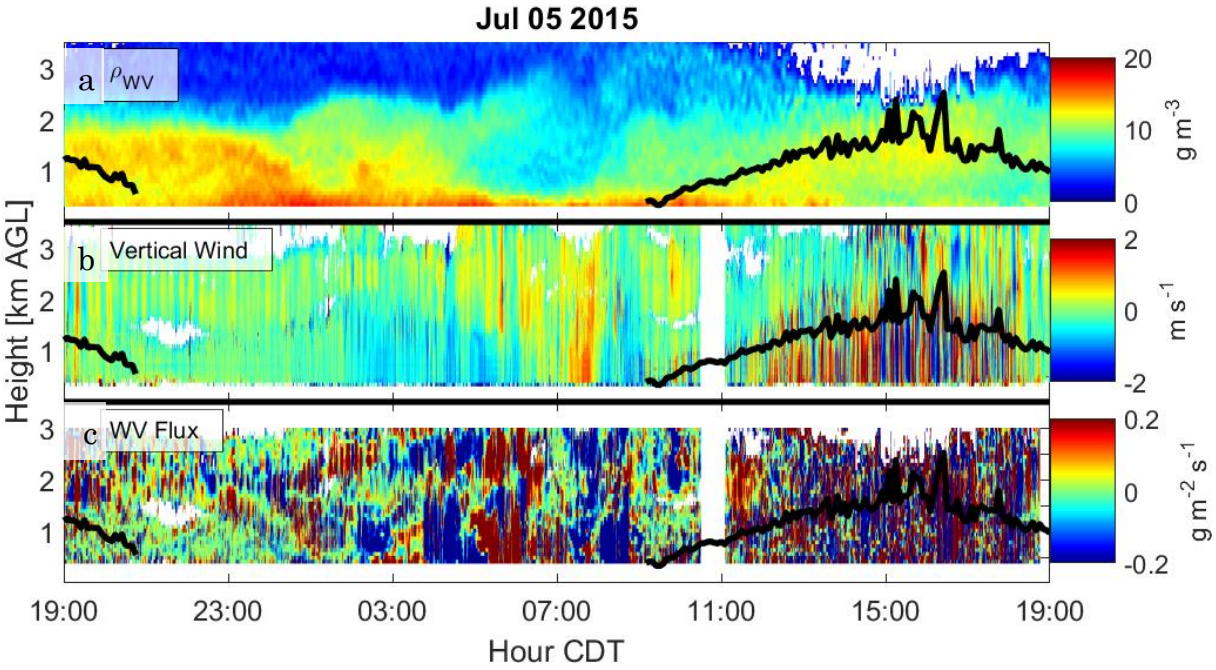

Figure 2.6. Evolution of profiles of water vaper, vertical wind, and water vapor flux from 19 CDT July 4th – 19 CDT July 5th. White spaces indicate regions of missing data. Black lines indicate the calculated depth of the boundary layer.

feature of interest can be seen in Fig. 2.6c, at about 1700 CDT between 1.50-2.25 km above ground level (AGL). Here, there are a number of gaps where the optically thick clouds have formed, leading insight into the profile of water vapor flux in a region of the atmosphere where cloud formation may likely occur. Towards the higher altitudes in this region, the red colors indicate a strong positive water vapor flux, indicating that this region has upward moving air with increasing moisture, or downward moving air with decreasing moisture. Right below these regions, the blue colors may indicate upwards moving air that is drying, as more and more moist eddies are being forced into the upper regions of the boundary layer. This "drying" could also be due to clouds nearby condensing into liquid water, thus decreasing the water vapor that is being detected by the DIAL.

2.3.5 Frequency Analysis

Turbulence spectra are used to study the distribution of turbulent eddies throughout the atmosphere. Eddy size is greatly influenced by a number of parameters, including wind speed, stability, boundary layer height, canopy height, and topography. The actual shape of the spectra is used to infer a number of characteristics about the measurements used for flux analysis. The shape of the spectrum is used to represent the cascade of largest eddies into the inertial subrange. The largest eddies contain the most energy, but cannot sustain their size, thus frequency spectra reveal these larger eddies breaking into smaller, more stable eddies within the inertial subrange. These larger eddies are also known as the integral turbulence scale, as they mark the region of energy in the spectra where turbulent production dominates (Kolmogorov 1941a,b).Beyond the 'knee' in the spectral plot, for frequencies lower than the highest magnitude, mesoscale effects such as the diurnal cycle are often responsible for these higher energy points. Within the inertial subrange, eddies should follow a slope of $f^{-5/3}$ as can be seen from daytime unstable conditions in Fig. 2.7a. As energy cascades into higher frequency eddies, energy becomes dissipated to thermal energy. Typically, this occurs in frequencies of 10-30 Hz, which is not shown in Fig 2.7 because the instrument resolution is 30 seconds (Foken and Nappo 2008). The overall contribution of these smaller eddies to the flux is very small and often negligible, as spectrums including these frequencies show that these eddies contain the least energy (Foken and Nappo 2008; Stull 1988).

Another interesting characteristic of turbulence spectra is their ability to show the shift in energy distribution as a result of a changed environmental factor. In Fig. 2.7a, the turbulence spectrum shows a very clear pattern, cascading at a slope of $f^{-5/3}$ from the integral scale to the highest frequencies. For the nighttime, stable case in Fig. 2.7b, a different pattern is seen. The peak in this power spectrum shifts to a lower frequency, and the average spectrum seems to hit a frequency knee around 9×10^{-3} Hz. This is likely due to the different mechanisms that allow the instruments to measure data effectively. At night, the water vapor DIAL becomes more accurate at measuring water vapor density as error due to solar background is removed. This is because the DIAL is an active remote sensing system, which uses backscatter at a wavelength centered on a water vapor band, and slightly offset from this band, to determine a water vapor profile. During the daytime, the sun emits radiation at a spectrum which has some overlap with the DIAL, therefore at night when the sun is blocked, this solar background can no longer introduce noise and error to the calculation of water vapor (Spuler et al. 2015). Also, the stable nature of the nocturnal boundary layer causes fewer cases of optically thick clouds to be present, also aiding the DIAL in measuring with higher accuracy at higher altitudes. The collapse of the daytime convective boundary layer allows for cleaner air, with fewer aerosols present to descend closer to the surface. This aids in measurements made with the DIAL. The radar wind profiler cannot measure as accurately. This is because the radar wind profiler relies on Bragg scattering to accurately estimate three-dimensional winds within the troposphere. As a result,

longer observation periods are needed by the radar wind profiler in order to accurately measure winds at night. As can be seen in the 30-s turbulent wind spectra, the radar wind profiler was unable to capture turbulence effectively at night (Fig. 2.7d). As a result, the water vapor and latent heat flux profiles cannot be reliably calculated at night with these two instruments (Fig. 2.7f).

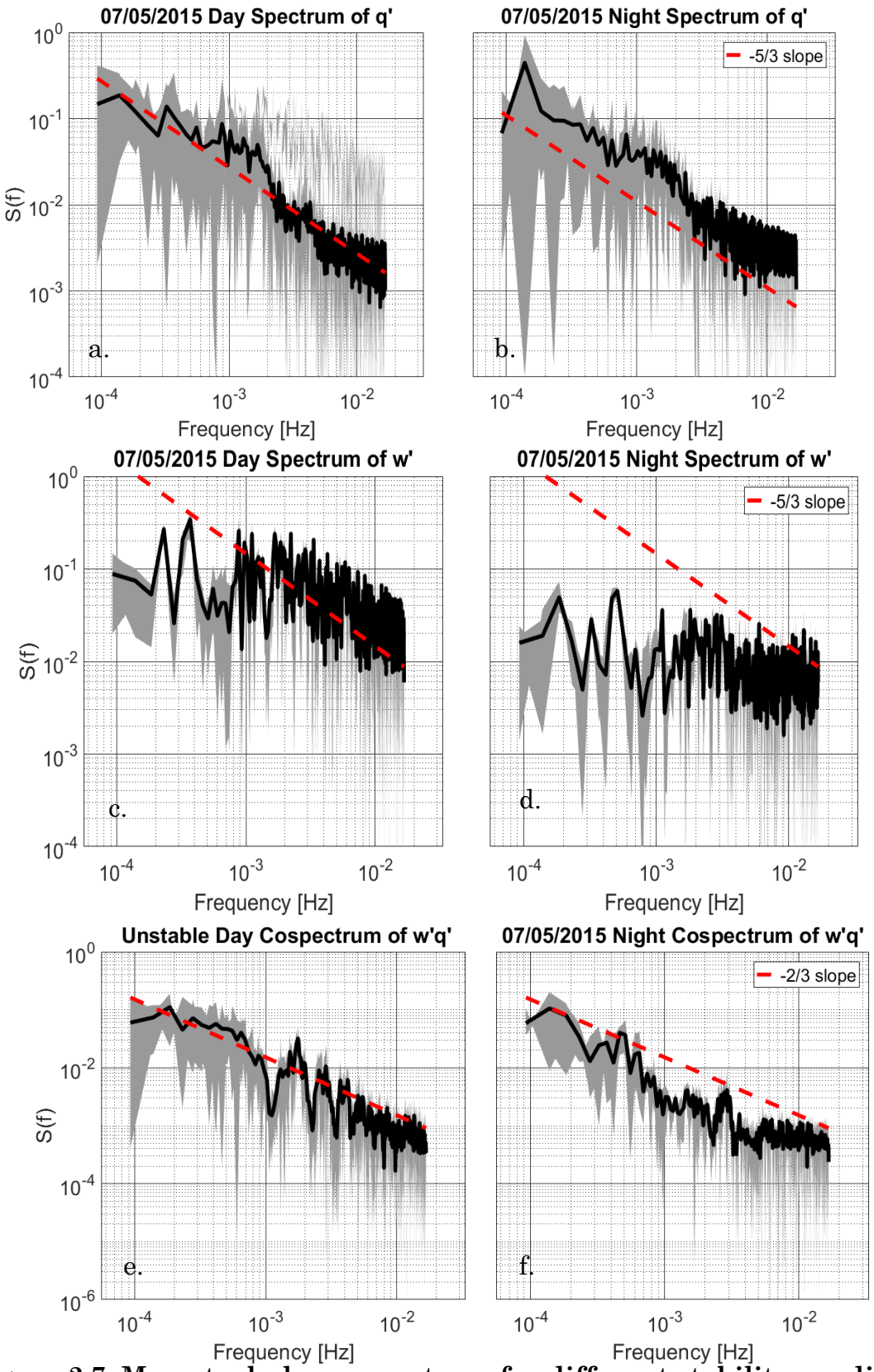

Figure 2.7. Mean turbulence spectrum for different stability conditions. The gray fill indicates the extent of the mean spectrums calculated from 300m to 2.5 km. Reynolds averaging period of 90 minutes is used.

The integral length scale was calculated for stable and unstable conditions, using a Reynolds averaging period of 90 minutes (Fig. 2.8) by finding the frequency corresponding to the peak magnitude in the turbulence spectrum, f_{max}. During the day, the water vapor spectra frequency ranged from 1.2×10^{-3} Hz to 5.6×10^{-4} Hz, with the highest frequencies seen near the surface. Similarly, day instantaneous wind spectra saw frequency maxes ranging from 1.2×10^{-3} to 3.2×10^{-4}. For night water vapor spectra, f_{max} ranged from 1.8×10^{-3} Hz to 1.9×10^{-4} Hz, with no clear pattern seen between the frequencies and height. No clear pattern was seen for instantaneous wind spectra f_{max} values as well, with all maximum frequencies for each altitude less than 8.0×10^{-4} Hz. All of these frequencies were within those seen in previous studies, which are typically on the order of 1×10^{-4} Hz (Kaimal and Finnigan 1994). According to Taylor's frozen turbulence hypothesis (Taylor 1938),

$$k = \frac{f_{max}}{\overline{W}} \qquad \text{Eq. 2.6}$$

where k is the wavenumber, f_{max} is the frequency corresponding to the spectral peak, and $\overline{W}$ is the mean vertical wind speed. Rearranging this equation, λ_{max}, the integral length scale, can be solved as:

$$\lambda_{max} = \frac{\overline{W}}{f_{max}} \qquad \text{Eq. 2.7}$$

For daytime instantaneous water vapor, the integral length scale ranged from approximately 4 km within the first 600 m of the troposphere, decreasing to

under 2 km as height increases to 3 km, as seen in Fig. 2.8c. For nighttime instantaneous water vapor values, length scales ranged from 2 km close to the surface, to approximately 500 m, with values varying from the kilometer to hundreds of meters scale intermittently, as seen in Fig. 2.8d. λ_{max} varied in this region until heights over 1 km were reached, where the lengths decreased to under 1 km further into the troposphere. The variability in length scale seen in the lower troposphere may be due to larger eddies being present in the middle of the boundary layer, where fewer sources of shear and/or friction are present. Between 600 m and 1.25 km, larger variability in the growth of the daytime boundary layer was observed, which may be why this region sees λ_{max} values range from a few hundred of meters to nearly 1.5 km. In higher regions of the troposphere, above the boundary layer, the vertical winds become much weaker, which is why length scales at these heights are much smaller. Additionally, the erratically large eddies in the lower portins of the boundary layer could be due to sampling error, as a result of the coarse temporal resolution of the profiling instruments being unable to capture many of the smaller eddies contributing to the formation of turbulent eddies.

Somewhat similar patterns are seen for the length scales observed for instantaneous vertical wind turbulence spectra. For daytime values, λ_{max} was in the range of 300-500 m between the lowest range gate of the wind profiler (300m), to heights of 800m, as seen in Fig 2.8a. After this height, a λ_{max} peak of 1.2km was reached, before decreasing to the scale of tens of kilometers above 1.25 km height. It is interesting to note that for daytime values, both instantaneous water vapor

and wind saw a peak in λ_{max} between 800 m and 1.2 km heights. This seems to be best attributed to interactions with the growing boundary layer into higher, drier portion of the troposphere, as this region saw the most changes associated with the growth and decay of the boundary layer height during the day. However, one would have expected a vertical profile of λ_{max} more similar to that seen with the radar wind profiler, with smaller eddies closest to the surface. The reason for the λ_{max} for instantaneous water vapor below 500 m is not immediately clear, but may be due to some error in the calculation of turbulence power spectra in this region, possibly due to the coarse temporal resolution unable to measure many of the smaller turbulent eddies present. Larger scale variations may have caused a lower frequency to hold more power than would be expected, therefore causing a much lower frequency than expected to be attributed to f_{max}. During nighttime, instantaneous wind λ_{max} does not see a clear pattern, with λ_{max} values varying between nearly 1 km and a few hundred kilometers between 300 m and 2.5 km AGL, as seen in Fig. 2.8b. Similarly, to the analysis for λ_{max} performed with water vapor, this is likely due to turbulence at night being more sporadic. Additionally, less moisture present in the atmosphere at night makes the radar wind profiler more error prone, as there is much less signal for the radar wind profile to measure Bragg scattering from.

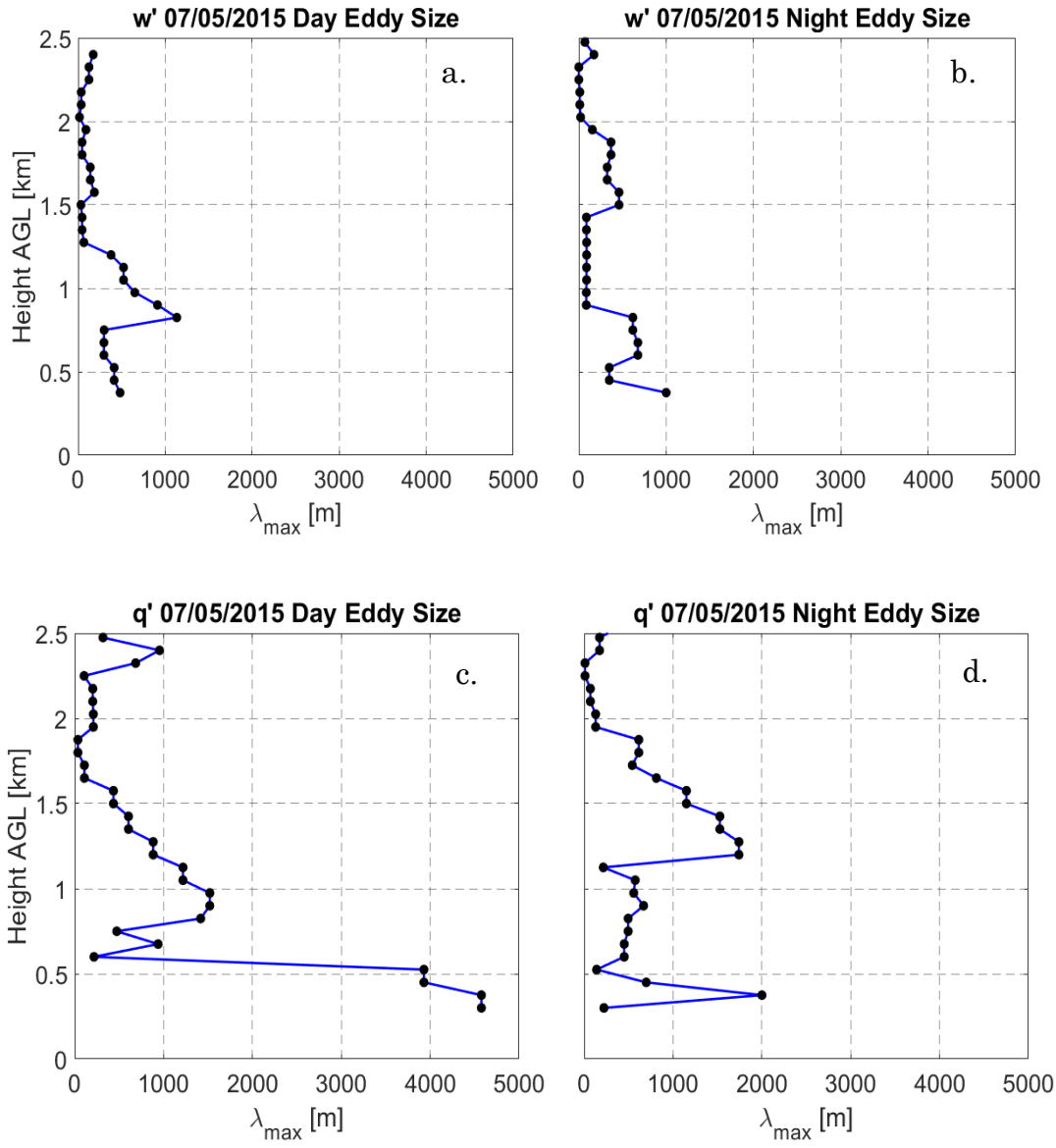

Figure 2.8. Mean eddy size as a function of height.

2.4 Conclusions

Profiles of water vapor and wind were used to calculate water vapor flux profiles. A variety of Reynold's averaging periods were tested in order to determine the optimal averaging period for calculating fluxes within regions of the boundary layer

above the surface layer. Both the method of Ogives as well as the method of flux normalization showed that daytime unstable conditions need to be averaged for at least 90 minutes between 300 m and the top of the convective boundary layer, which agrees well with previous studies using both tall towers and profiling instruments (Berger et al. 2001; Linné et al. 2007). Current analysis showed tilt angles corrected by 1-1.5° in the *X-Z* and *Y-Z* planes, thus confirming the necessity to apply a rotation correction to the dataset. Very large differences were seen when comparing rotated and non-rotated data for stable nighttime conditions. The reason for this discrepancy may lie in turbulence being more intermittent during stable conditions. The integral length scale corresponding to vertical velocity yielded eddies on the order of hundreds of meters, with a maximum in length seen in the region of the atmosphere which experienced the most rapid changes in daytime boundary layer depth. No clear pattern was seen in the size distribution of eddies at night, while both instantaneous water vapor and wind data revealed maxima corresponding to the portions of the atmosphere where the boundary layer varied the greatest during the day.

The analysis performed in this chapter was able to successfully characterize turbulence within the boundary layer during daytime, unstable conditions. Eddies within the convective boundary layer were seen to have very similar characteristics in terms of optimal averaging period and integral length scale. Therefore, these observations are able to confirm theoretical profiles of turbulence (Stull 1988; Lee et al. 2006). However, future work using a longer period of time, as well as studying

the effect of heterogeneous topography will allow for a greater understanding of turbulence in the boundary layer above the surface layer. Work was done to compare the correlation of 8.5 m and 300 m water vapor flux during day and night conditions, but R^2 values for these tests were less than 0.1. In chapter three, the reasoning for this discrepancy is explored.

2.5 Chapter Two References

Angevine, W. M., A. B. White, and S. K. Avery, 1994: Boundary-layer depth and entrainment zone characterization with a boundary-layer profiler. Boundary-Layer Meteorol., **68**, 375–385.

Aubinet, M., B. Heinesch, and B. Longdoz, 2002: Estimation of the carbon sequestration by a heterogeneous forest: Night flux corrections, heterogeneity of the site and inter-annual variability. Glob. Chang. Biol., **8**, 1053–1071.

Bakwin, P. S., P. P. Tans, D. F. Hurst, and C. Zhao, 1998: Measurements of carbon dioxide on very tall towers: results of the NOAA/CMDL program. Tellus B, **50**, 401–415.

Baldocchi, D., E. Falge, L. Gu, R. Olson, and others, 2001: FLUXNET: A new tool to study the temporal and spatial variability of ecosystem-scale carbon dioxide, water vapor, and energy flux densities. Bull. Am. Meteorol. Soc., **82**, 2415.

Berger, B. W., K. J. Davis, C. Yi, P. S. Bakwin, and C. L. Zhao, 2001: Long-term carbon dioxide fluxes from a very tall tower in a northern forest: flux measurement methodology. J. Atmos. Ocean. Technol., **18**, 529–542.

Blanken, P. D., 1998: Turbulent Flux Measurements Above and Below the Overstory of a Boreal Aspen Forest. Boundary-Layer Meteorol., **89**, 109–140, doi:10.1023/A:1001557022310. http://dx.doi.org/10.1023/A:1001557022310.

Davis, K. J., P. S. Bakwin, C. Yi, B. W. Berger, C. Zhao, R. M. Teclaw, and J. G. Isebrands, 2003: The annual cycles of CO2 and H2O exchange over a northern mixed forest as observed from a very tall tower. Glob. Chang. Biol., **9**, 1278–1293.

Deacon, E. L., and E. B. Kraus, 1968: The levelling error in Reynolds stress measurement. Bull. Am. Meteorol. Soc, **49**, 836.

Desai, A. R., and Coauthors, 2015: Landscape-level terrestrial methane flux observed from a very tall tower. Agric. For. Meteorol., **201**, 61–75.

Desjardins, R. L., J. I. MacPherson, P. H. Schuepp, and F. Karanja, 1989: An evaluation of aircraft flux measurements of CO2, water vapor and sensible heat. Boundary Layer Studies and Applications, Springer, 55–69.

Dyer, A. J., 1981: Flow distortion by supporting structures. Boundary-Layer Meteorol., **20**, 243–251.

Ehret, G., K. P. Hoinka, J. Stein, A. Fix, C. Kiemle, and G. Poberaj, 1999: Low stratospheric water vapor measured by an airborne DIAL. J. Geophys. Res.

Atmos., **104**, 31351–31359.
Foken, T., and C. J. Nappo, 2008: Micrometeorology. Springer Science & Business Media,.
Giez, A., G. Ehret, R. L. Schwiesow, K. J. Davis, and D. H. Lenschow, 1999: Water vapor flux measurements from ground-based vertically pointed water vapor differential absorption and Doppler lidars. J. Atmos. Ocean. Technol., **16**, 237–250.
Kaimal, J. C., and D. A. Haugen, 1969: Some errors in the measurement of Reynolds stress. J. Appl. Meteorol., **8**, 460–462.
Kaimal, J. C., and J. J. Finnigan, 1994: Atmospheric boundary layer flows: their structure and measurement. Oxford University Press,.
Kiemle, C., G. Ehret, A. Giez, K. J. Davis, D. H. Lenschow, and S. P. Oncley, 1997: Estimation of boundary layer humidity fluxes and statistics from airborne differential absorption lidar (DIAL). J. Geophys. Res. Atmos., **102**, 29189–29203.
——, and Coauthors, 2007: Latent heat flux profiles from collocated airborne water vapor and wind lidars during IHOP_2002. J. Atmos. Ocean. Technol., **24**, 627–639.
Kolmogorov, A. N., 1941a: Dissipation of energy in locally isotropic turbulence. Dokl. Akad. Nauk SSSR, Vol. 32 of, 16–18.
Kolmogorov, A. N., 1941b: The local structure of turbulence in incompressible viscous fluid for very large Reynolds numbers. Dokl. Akad. Nauk SSSR, Vol. 30 of, 301–305.
Lee, X., W. Massman, and B. Law, 2006: Handbook of micrometeorology: a guide for surface flux measurement and analysis. Springer Science & Business Media,.
Lindseth, B., W. O. J. Brown, J. Jordan, D. Law, T. Hock, S. A. Cohn, and Z. Popovic, 2012a: A New Portable 449-MHz Spaced Antenna Wind Profiler Radar. IEEE Trans. Geosci. Remote Sens., **50**, 3544–3553.
——, T. Kelly, W. O. J. Brown, T. Hock, S. A. Cohn, and Z. Popovic, 2012b: Low-cost 63% efficient 2.5-kW UHF power amplifier for a wind profiler radar. Microwave Symposium Digest (MTT), 2012 IEEE MTT-S International, 1–3.
——, W. O. J. Brown, T. Hock, S. A. Cohn, and Z. Popović, 2014: Wind profiler radar antenna sidelobe reduction. IEEE Trans. Antennas Propag., **62**, 56–63.
Linné, H., B. Hennemuth, J. Bösenberg, and K. Ertel, 2007: Water vapour flux profiles in the convective boundary layer. Theor. Appl. Climatol., **87**, 201–211.
Senff, C., J. Bösenberg, and G. Peters, 1994: Measurement of water vapor flux profiles in the convective boundary layer with lidar and radar-RASS. J. Atmos. Ocean. Technol., **11**, 85–93.
Spuler, S. M., K. S. Repasky, B. Morley, D. Moen, M. Hayman, and A. R. Nehrir, 2015: Field-deployable diode-laser-based differential absorption lidar (DIAL) for profiling water vapor. Atmos. Meas. Tech., **8**, 1073–1087.
Stull, R. B., 1988: An introduction to boundary layer meteorology. Springer Science & Business Media,.
Taylor, G. I., 1938: The spectrum of turbulence. Proceedings of the Royal Society of

London A: Mathematical, Physical and Engineering Sciences, Vol. 164 of, 476–490.

Wilczak, J. M., S. P. Oncley, and S. A. Stage, 2001: Sonic anemometer tilt correction algorithms. Boundary-Layer Meteorol., **99**, 127–150.

Willis, G. E., and J. W. Deardorff, 1976: On the use of Taylor's translation hypothesis for diffusion in the mixed layer. Q. J. R. Meteorol. Soc., **102**, 817–822.

Wulfmeyer, V., 1999: Investigation of turbulent processes in the lower troposphere with water vapor DIAL and radar-RASS. J. Atmos. Sci., **56**, 1055–1076.

Wulfmeyer, V., S. K. Muppa, A. Behrendt, E. Hammann, F. Späth, Z. Sorbjan, D. D. Turner, and R. M. Hardesty, 2016: Determination of convective boundary layer entrainment fluxes, dissipation rates, and the molecular destruction of variances: theoretical description and a strategy for its confirmation with a novel lidar system synergy. J. Atmos. Sci., **73**, 667–692.

CHAPTER THREE

A Case Study of Water Vapor Flux Profiles

3.1 Introduction

The main goal of the PECAN field campaign was to advance understanding and forecast skill of the processes that initiate and maintain nocturnal convection in the Great Plains. Four main objectives were studied during this campaign, including initiation and evolution of elevated convection, internal structure and microphysics of mesoscale convective systems (MCSs), bores and wave-like features which occur near MCSs, and the structure and evolution of the Great Plains Nocturnal Low-Level Jet (NLLJ) (Geerts et al. 2016). The analysis performed in this thesis was gathered from instruments deployed at a fixed site, which were meant to study atmospheric thermodynamics and boundary layer dynamics as these four atmospheric phenomena occurred near the site. The work done in this thesis seeks to add further understanding to mechanisms of turbulence, convective boundary layer dynamics, and convective initiation, and can be potentially used to study and analyze patterns of turbulence during the afternoon-evening transition. The PECAN field campaign collected data from collocated profiling instruments, including a flux tower, water vapor DIAL, and radar wind profiler which were operational for an extended period of time (6 weeks). This wealth of data allowed for

the relationship between surface and elevated water vapor flux measurements (above 300 m) to be studied for many different stability conditions, as well as under the influence of different atmospheric phenomena. As a results this chapter walks through a case study of three days, in which different phenomena are observed to interact with turbulent features and convective boundary layer growth. This chapter seeks to establish how calculations of water vapor fluxes and latent heat fluxes between 300 m and the height of the convective boundary layer can yield further understanding of turbulent dynamics which has not been possible before.

For this chapter, a set of days from 6/21/2015 to 6/24/2015 were chosen to be analyzed. This was because this time period included two days with clear skies, afternoon boundary layer convection, and boundary layer height development greater than 1 km in Kansas during the summer, in addition to a day in which stable conditions, and stagnated boundary layer growth was observed. On 6/22/2015, boundary layer growth stagnation may have been due to the presence of an unusually strong nocturnal low level jet the night of 6/21-6/22. During the daytime of 6/22, the boundary layer growth stagnated after noon, which may have been due to more stable conditions being present, with warm, moist air present aloft during the morning and early afternoon hours. The study of these three full days together allowed an examination of patterns of water vapor and water vapor flux change between unstable, convective conditions and stable conditions with inhibited boundary layer growth. Causes for the differences are observed using calculated

flux footprints, water vapor flux divergence, and the influence of meteorological parameters at the surface and within the atmosphere.

Additionally, this chapter explores how source areas measured by the profilers and flux towers change with height. This footprint analysis is useful, as it provides insight as to how large of a area that a sensor is observing at different heights and if measurements made at different heights should be expected to be somewhat related. This is important for relating measurements made by the 8.5 m flux tower and 300 m range gate of the DIAL and AERI, as the footprints being sampled by these types of instruments could be completely different.

The role of convergence and divergence of water vapor within the convective boundary layer is also studied in this chapter. The flux convergence, calculated in a water vapor flux profile for one point in time can actually serve as a predictor as to if a profile will be expected to moisten or dry over time. This tool, derived from water vapor flux measurements, could be used for future studies to analyze how patterns in turbulence could be related to the occurrence of convective initiation. The applicability and limitations of calculating flux divergence in water vapor flux profiles are discussed later in this chapter.

3.2 Methods

3.2.1 Flux Footprint Calculation

Flux footprint modelling is a method used by micrometeorologists for the purpose of quantifying the upwind source area that contributes to a turbulent flux measurement. The flux footprint itself has been defined as “the effective upwind

source area sensed by the observation" (Leclerc and Thurtell 1990; Schuepp et al. 1990). The source area being measured at the point of observation is heavily dependent on meteorological conditions, as well as topographical features. As a result, footprint models use a combination of meteorological and surface based parameters, as well as statistical dispersion functions, to approximate the source area of a particular observation.

For this project, results from running a backward Lagrangian dispersion model (LPDM) are used to estimate the flux footprint of the measurements (Kljun et al. 2015). This model was run under a variety of meteorological and surface characteristics in order to construct a parameterized footprint function. This resultant parameterized function reduces the need for a supercomputer, as it uses the results of a multitude of simulations to infer patterns in the shape and structure of the flux footprint. Over 200 simulations were run to determine the coefficients used in parametrized footprint equations (Kljun et al. 2015).

Kljun's 2-dimensional model is also particularly useful as it has been used to estimate the flux footprint under a wide variety of stability conditions and receptor heights, which has been difficult with previous models (Kormann and Meixner 2001; Schmid and Oke 1990; Schmid 1994, 1997). Therefore, the utility of Kljun's model will be used to determine how different source areas dominate when looking at measurements within different regions of the convective boundary layer. This is of particular interest for this analysis, as the measurements made in the lowest portion of the boundary layer were made at the Millersville University flux tower,

while measurements above 300 m are calculated using the WV-DIAL and 449 MHz wind profiler. In order to relate these two measurements from different heights, the flux footprint must be evaluated. This will allow one to discern if the source area of both measurements is comparable, and if discrepancies seen between the two datasets can be explained by different source regions.

The flux footprint equation used takes the following form:

$$f(x,y)=\overline{f^{y}(x)}\frac{1}{\sqrt{2\pi}\sigma_y}e^{-\frac{y^2}{2\sigma_y^2}} \quad \text{(Eq.3.1)}$$

In Eq. 3.1, $\overline{f^{y}(x)}$ is the crosswind integrated footprint function, σ_y is the standard deviation of the crosswind distance, x is the along-wind distance from the receptor, and y is the cross-wind distance from the receptor. $x = y = 0$ is the location of the receptor. Kljun (2015) goes step-by-step in the derivation of this equation, as $\overline{f^{y}(x)}$ and σ_y are determined using the results of the runs of the LPDM by fitting the data to functions based on previous work (Pasquill and Smith 1983; Horst and Weil 1992; Weil and Horst 1992; Deardorff and Willis 1975). The resulting footprint calculation was fed into a MATLAB script under a variety of meteorological and stability conditions during the PECAN 2015 field campaign. This script was combination of Klujn's code, and script that I wrote myself to specifically analyze how meteorological conditions present during the PECAN field campaign could alter the calculated flux footprint at different heights observed by the flux tower and profiling instruments. This resulting script determines the shape of the footprint, as well as the relative contribution of the surrounding sources to the total footprint area. The relative contribution serves as a way of visualizing and

analyzing how the footprint changes in time as well as receptor height, by drawing out ellipses, which encompass different percentages of the total footprint area. In this analysis, the 80% relative contribution to the total footprint was used as the Gaussian shape of the footprint causes the amount of contribution to decrease rapidly as a function of distance from the receptor. Therefore, 80% allows for the main shape of the footprint to be captured. The relative contribution to the total footprint is calculated by integrating from the footprint peak location into all directions along constant levels of footprint values until the contribution of interest is obtained. This is possible, as the complete integration of the footprint would be 100%; therefore, integrating the footprint until 0.80 is reached would yield 80% of the footprint, and its associated shape.

The flux footprint calculated is taken as the 1 hour average of meteorological data centered at the hour of interest. For footprints calculated using the collocated profilers, meteorological data is additionally averaged for 75 m above and below the height of interest, for a total of 150 m spatial averaging.

3.2.2 Latent Heat Flux Calculations

The latent heat flux is used to measure the energy required (or released) due to the phase change of water within the convective boundary layer. This measurement is analogous to water vapor flux, except it is measured in units of power per meter squared, instead of mass per meter squared per second. To calculate the latent heat flux, Atmospheric Emittance Radiance Interferometer (AERI) temperature and pressure profiles were used (Turner and Löhnert 2014) in

addition to the water vapor and and profiles from the water vapor DIAL and 449 MHz radar wind profiler, respectively. Information from temperature profiles are necessary to calculate latent heat flux in order to convert from water vapor density to latent heat, as seen in Eq. 3.2. Because the statistical retrieval algorithm of the AERI limits the temporal resolution to 5 minutes, average values of temperature are used to approximate the latent heat flux. Unfortunately, the 5 min temporal resolution of this instrument prevents an accurate calculation of sensible heat flux, therefore only water vapor and latent heat flux will be studied in this analysis. Eq. 3.2 demonstrates the how measurements of AERI temperature data are used to calculate the instantaneous latent heat, with units of W m^{-2}, using the equation for latent heat of vaporization provided by Stull, 1988.

$$LH = (2.501 - 0.00237 \times T_{AERI}) \times 10^3 \times \rho_{H_2O} \qquad \text{Eq.3.2}$$

A positive latent heat flux will occur when air is moistening and rising at the same time, during convective conditions, and/or descending and drying. Likewise, a negative heat flux will occur if air is rising and drying, or descending and moistening, such as when dew occurs as night.

3.2.3 Water Vapor Flux Divergence Calculations

Calculating the divergence within a water vapor flux profile allows for one to study how the vertical movement of water vapor is changing over time. This calculation uses water vapor flux calculated using the water vapor DIAL and radar wind profiler. In simplest terms, the divergence is measured as the negative slope of the water vapor flux profile. Total divergence is given by the following equation:

$$\mathrm{div}(\bar{q}) = \frac{d\bar{q}}{dt} + \bar{u}\frac{d\bar{q}}{dx} + \bar{v}\frac{d\bar{q}}{dy} + \frac{d\overline{w'q'}}{dz} = 0 \qquad \text{(Eq. 3.3)}$$

In the aforementioned equation, $\bar{u}$, $\bar{v}$, and $\bar{w}$ represent the average vector wind speeds in the stream wise (x), crosswind (y), and vertical (z) directions respectively, $\bar{q}$ is the average water vapor, and $\overline{w'q'}$ is the water vapor flux. (Kiemle et al. 2007; Stull 1988; Giez et al. 1999). In situations where horizontal advection is minimal, this equation can be reduced to:

$$\frac{d\bar{q}}{dt} = -\frac{d\overline{w'q'}}{dz} \qquad \text{(Eq. 3.4)}$$

Thus, the change in water vapor over time in a specific region in the column being measured is approximately equal to the negative slope of the water vapor flux within a specified region of the vertical column.

A negative divergence value indicates convergence, or moistening of the section of a profile over a period of time. This pattern is often seen during daytime, convective conditions, as eddies will rise from the surface, moistening higher altitudes with water vapor provided by evapotranspiration at the surface. A water vapor profile will typically have a negative slope, approaching 0 near the cloud base height. If cloud formation is occurring, the water vapor flux will become negative, and continue to follow a negative slope. However, instrument limitations of the DIAL prevent liquid water from being measured. Therefore, one often sees a highly erratic water vapor flux profile near the location of clouds in the profile.

Likewise, a positive value for divergence will indicate that drying is occurring. This can happen if water with little moisture is subsiding, adiabatically drying as it descends. Additionally, if the moisture source near the surface is

depleted, dry eddies will rise through the atmosphere, leading to the air closest to the surface becoming drier in the later afternoon hours.

The moisture flux divergence calculated from profiing instruments during the late morning/early afternoon can provide a predictor for whether the convective boundary layer will moisten or dry at later times. This is because the moisture flux divergence is representative of the rate of change of moisture within the convective boundary layer. This pattern, however, only serves as a short-term trend, and should therefore be interpreted on the scale of 1-3 hours from the time the flux profile was measured. This calculation could prove to be useful for the PECAN field campaign, as it provides a new method to study the vertical movement of water vapor in a pre-convective environment, as well as how water from larger source areas are being used to moisten the convective boundary layer.

3.3 Results

3.3.1 Conditions Observed June 21st – 23rd, 2015

Fig. 3.1-3.4 provides an overview of the meteorological conditions present from 6/21/2015-6/23/2015. No intensive observation period (IOP) was performed the night of 6/20-6/21, but an unofficial field operation (UFO) was performed to monitor the afternoon to evening wind transition as well as the possibility of convective initiation. A surface cold front was observed during the evening moving southwestward past Ellis, Kansas. This feature was able to generate a few convective cells in the evening hours, before weakening and dissipating overnight. Between 0400 and 0800 CDT on 6/21, strong low level winds existed within 500 m of

the surface, likely related to a southwesterly low-level jet (Fig. 3.4c). In the early morning hours of 6/21, a brief wind shift near the surface was observed (Fig. 3.4d), before winds weakened during the day and boundary layer convection commenced. In Fig. 3.2a, one can observe the drops in incoming shortwave radiation as clouds passed overhead. During the afternoon-evening transition, as afternoon convection dissipated, strong southerly winds began to take hold, as seen in Fig. 3.4d.

The night of 6/21-6/22 saw one of the strongest Nocturnal Low-Level Jets (NLLJ) form of the PECAN 2015 field campaign. This ribbon of fast moving, moist air had maximum wind speed near the surface in excess of 30 m/s, with a feature of strong wind extending to nearly 3 km, according to the 449 MHz wind profiler, as can be seen in Fig. 3.4c. Another interesting feature seen this night were the small plumes of upward moving air, directly above the NLLJ, which was likely due to the warm, buoyant elevated air ascending through the cooler nighttime air mass above it (Fig. 3.4e). The temperature differences between the warm air advected by the LLJ can also be seen in the overnight AERI data, with very warm temperature, nearing 30°C in the core of the LLJ approximately 1 km AGL at 0800 CDT. During the day on 6/22, clear-air convection and boundary layer growth was much weaker than that observed on 6/21. This may have been partially due to the cooler surface temperature observed. Surface energy flux measurements, in Fig. 3.2, show that there was nearly the same amount of solar radiation as the previous day, but an increased amount of sensible and latent heat fluxes. The decrease in daytime surface temperatures may have been due to a daytime shift in wind direction, from

a warm, southwesterly source to cooler, northerly source, as can be seen in Fig 3.3b and 3.4c-e. This cooler source of air may have caused the inhibited convection, and thus stagnated boundary layer growth observed. Greater stability during daytime conditions were observed, as can be seen in Fig 3.1. Therefore, the moisture and sensible heat fluxes observed would have allowed for the upward movement of air parcels, but their ascent would be limited by the stagnated boundary layer height, which may have caused the moist conditions observed in the afternoon and early evening seen on 6/22.

The night of 6/22-6/23 also proved to be quite interesting, though there was no IOP performed. A weak cold front, which moved southeast of Ellis, KS, caused for dry air near the surface to inhibit any convective cells from forming in the late evening and overnight. A plume of moist air was observed above the frontal boundary with clouds atop the moist boundary, as can be seen in Fig. 3.4a. The day of 6/23 saw fairly characteristic summertime convective conditions for Kansas, with the boundary layer increasing in depth through the afternoon and evening hours, before deteriorating as the sun went down. A couple of clouds were able to form as the product of late afternoon convection which can be seen in Fig. 3.2a.

These three days chosen in this case study are able to provide two days of unstable, convective conditions with limited cloud cover and one day of inhibited convection and less unstable conditions (6/22), as can be seen in Figs. 3.1 and 3.4. These dates were chosen because they are able to display how profiles of latent heat flux can be attributed to different changes in meteorological phenomena, both

during conditions with well understood convection, as well as conditions with less convective boundary layer growth than expected after a strong NLLJ event.

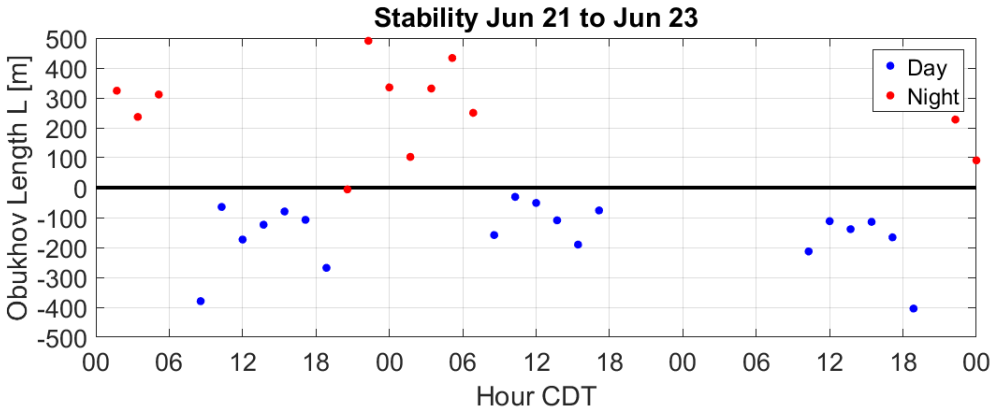

Figure 3.1 Obhukov length, indicative of atmospheric stability for the case study period.

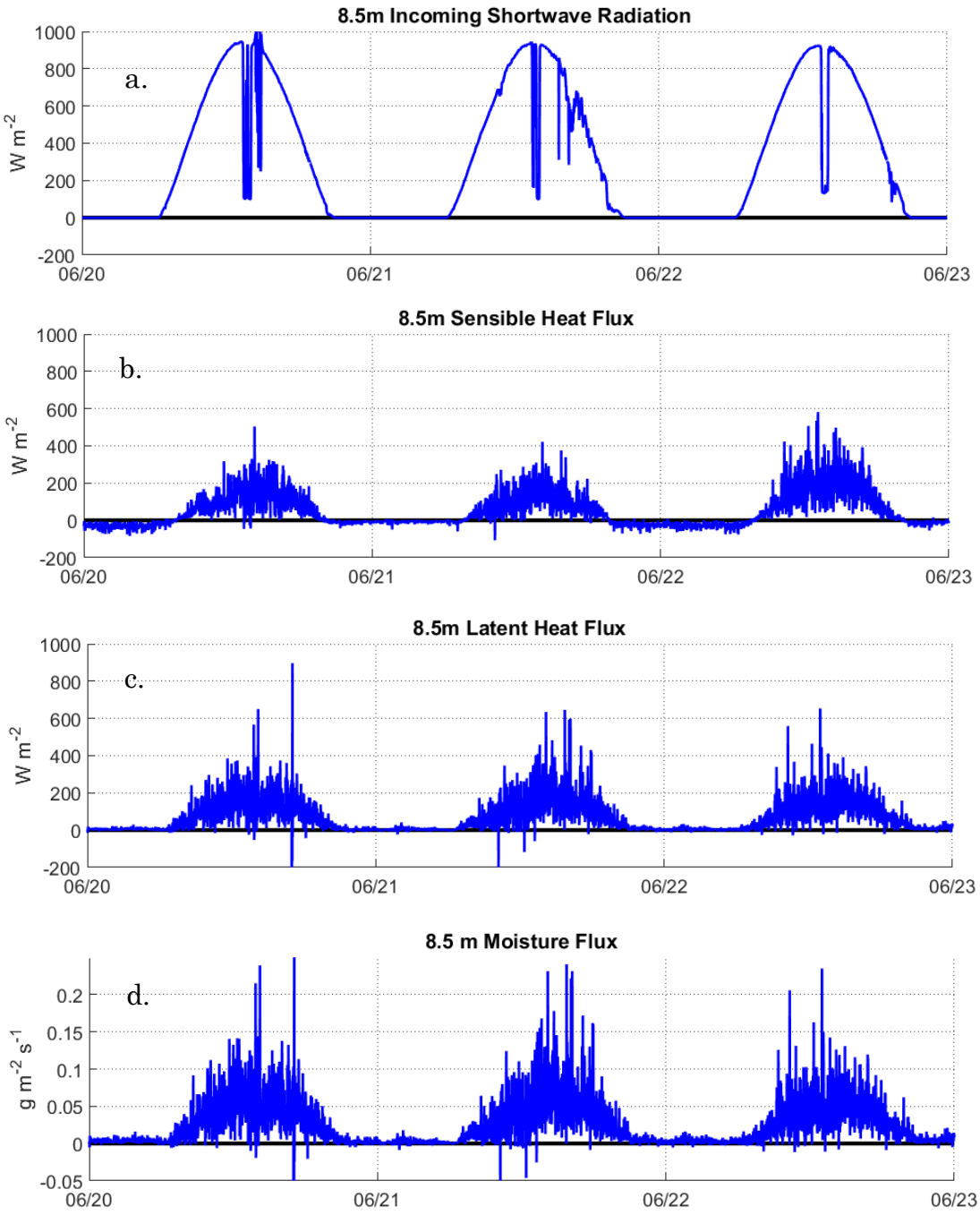

Figure 3.2. Flux measured at 8.5 km at the MU FP3 flux tower during the case study period.

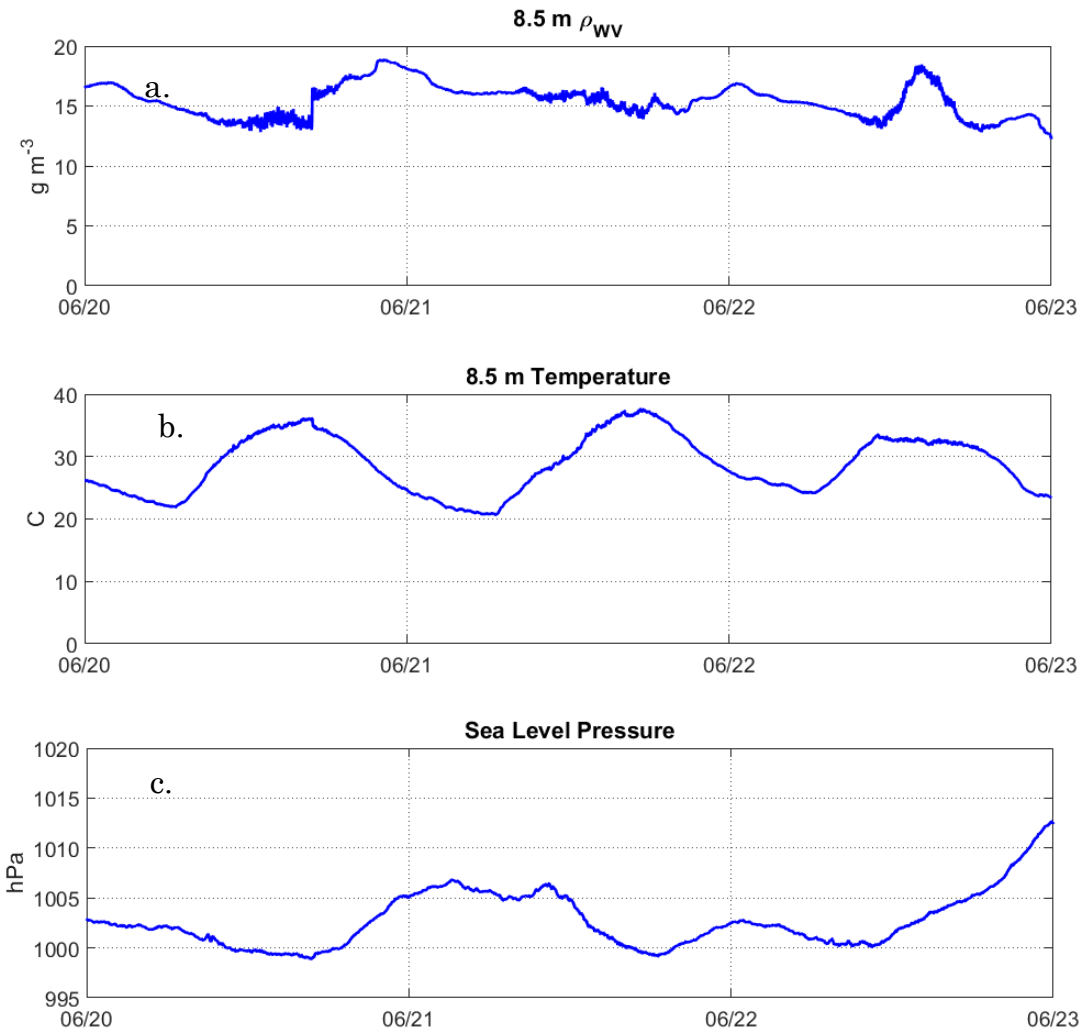

Figure 3.3. Meteorological parameters measured at MU FP3 flux tower. Pressure, in subpanel c, is also measured at 8.5 m, but corrected to sea-level pressure in order to relate better with meteorological phenomena.

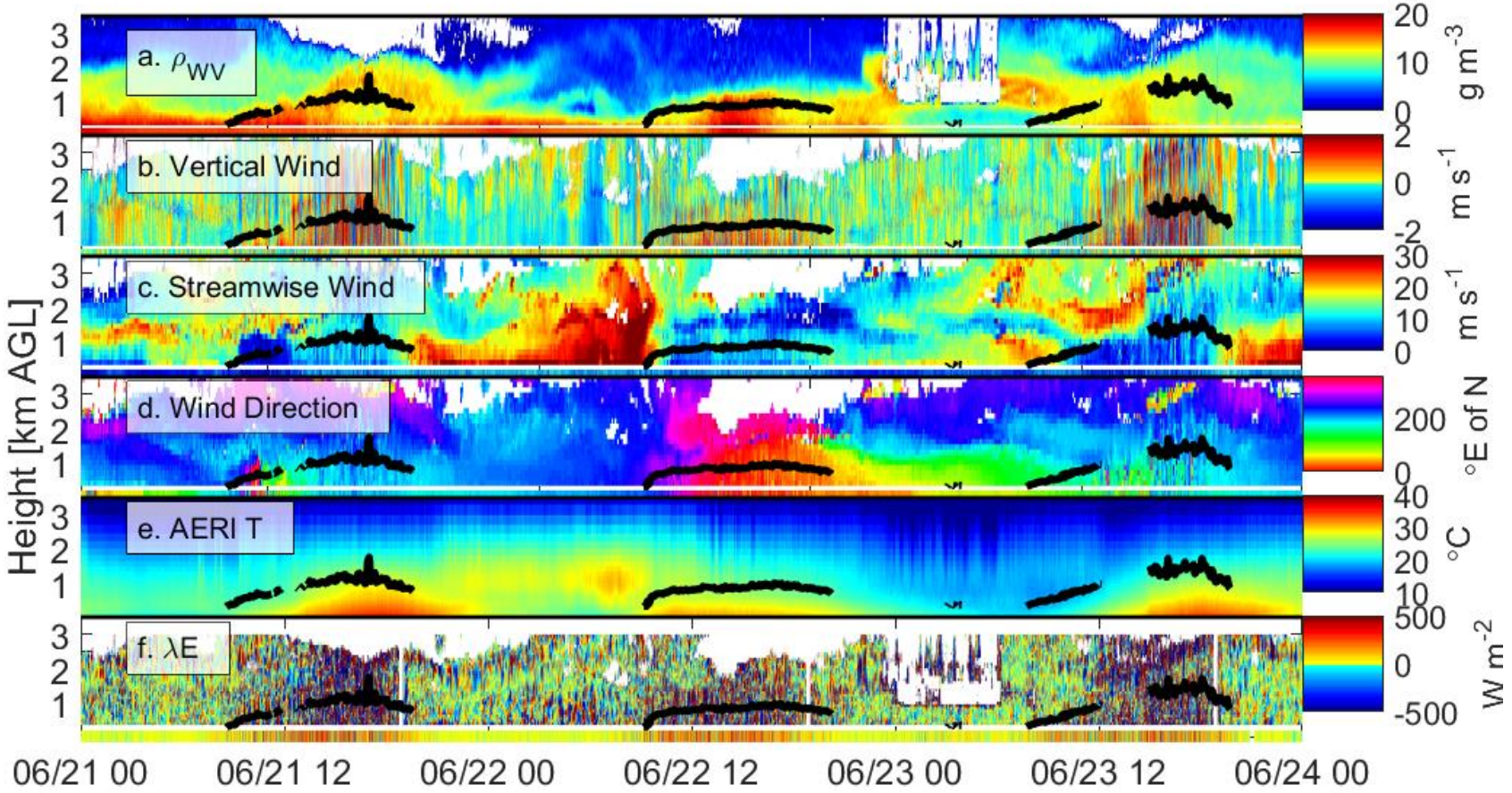

Figure 3.4. Profiles of meteorological phenomena observed during case study period, derived from (a) water vapor DIAL, (b,c,d) 449 MHz radar wind profiler, (e) AERI, and (f) water vapor DIAL and 449 MHz radar wind profiler. Surface data, taken from the NCAR met station and MU flux tower, represent the strip of data in the lowest altitude bin of the subpanels.

3.3.2 Evolution of Flux Footprint

The flux footprint was observed to change in time at fixed receptor heights, as well as by height at a fixed time. This can be seen in the first day observed in this case study, 6/21/2015 (Fig. 3.5). 6/21 was observed as a sunny summer day with a few clouds passing overhead, with surface temperatures reaching as high as 38°C, and relative humidity ranging from ~70% in the morning to ~30% in the late afternoon. These unstable, convective conditions allowed for a boundary layer to develop to a depth of 1 km during the day, with the boundary layer decreasing in the early evening as convection subsided. At around 1300 CDT, the winds near the surface were out of the southeast, which can be seen in the footprint of Fig. 3.5a. At this time, but higher in altitude, the wind shifts back to southerly by 800 m AGL. This vertical wind shear can be

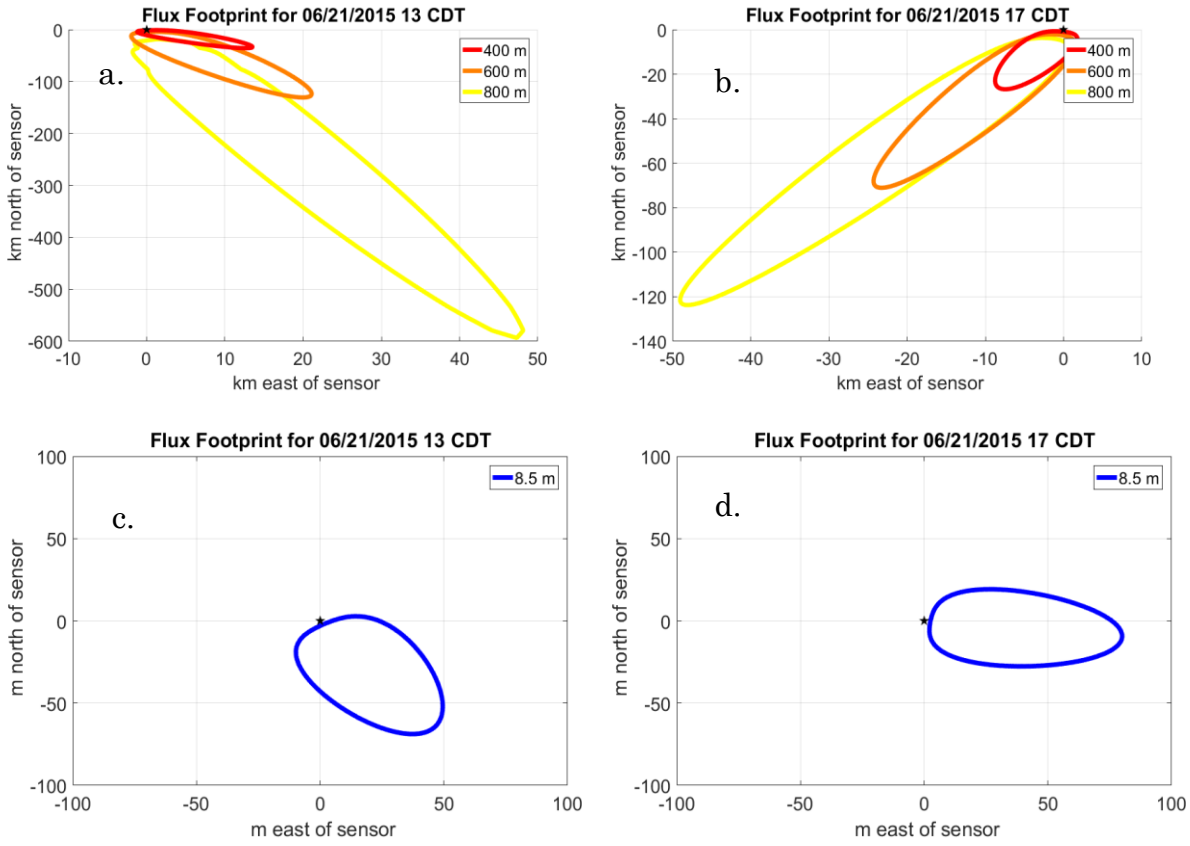

Figure 3.5 Evolution of flux footprints for 6/21/2016. Profiler footprints are shown in the top two plots, while the 8.5m footprint is shown on the bottom. Black star indicates location of sensor.

seen in Fig. 3.4d during the afternoon hours, with a southerly wind and eventually extending throughout the full profile. This shear is likely the cause of the shifts in height seen with the flux footprint of Fig. 3.5a and Fig 3.5c. By 1700 CDT, the surface footprint has a much more easterly component (Fig 3.5d), while the footprints at 400 m, 600 m and 800 m are more southwesterly (Fig. 3.5b). This shows that the measurements being made at higher altitudes at the location of the co-located radar wind profiler and WV lidar do not come from the same source as

the surface-based measurements at the FP3 site. This discrepancy is seen in a number of the footprints calculated, which could be why some of the surface measurements did not correlate well with measurements higher in the atmosphere made by the profilers.

The calculated footprints also show how the spatial scale differs greatly as the measurements are made at different heights. The flux measurements made at the MU site, at z = 8.5 m, tend to have a flux footprint on a scale of a couple of hundred meters. However, the measurements made by the collocated profiling instruments, with 300 m < z < 3000 m, will have a footprint whose 80% extent reaches tens to hundreds of kilometers as seen in Fig. 3.5a-b. This much larger footprint sensed by the profiling instruments will therefore also be representative of meteorological and topographical influences on this scale. The larger area surrounding both the NCAR and MU sites is dominated by agricultural activities, such as winter wheat and sorghum fields, and cattle pastures. However, the MU site is located just east of the town of Ellis, KS. The MU site is located near houses and town buildings, as well as a creek which is bordered by woody wetlands. Because of these differences in land cover type, the MU site is more likely to have an increased average roughness length and smaller footprint due to the taller obstructions near the site. The MU site will have roughness lengths (z_0) vary between 0.08 – 0.7 m, while the NCAR site will see a larger area with much less friction, and z_0 vary between 0.04 - 0.18 m, depending on crop type and harvest status (Wieringa 1992). The NCAR profilers are more likely to see the source of

water vapor flux originating from large areas, as well as advective processes, since there is a smaller influence of surface friction at measurements taken in the middle to upper boundary layer.

On 6/22, conditions were slightly cooler than the previous day, with just a few clouds passing over in the late afternoon. However, similar dew points to the prior day yielded higher levels of moisture in the boundary layer, which can be seen in Fig. 3.4a. Less boundary layer development is seen in the later afternoon as a result of reduced convection, with the depth of the boundary layer stagnating around 900 m after 1200 CDT. The shallower boundary layer allows for only the footprints at 400 m and 600 m AGL to be calculated, as the higher altitude studied, 800 m, is above the boundary layer for this day. At 1300 CDT, an easterly wind near the surface is seen to influence the footprint of the MU flux (Fig. 3.6c), while the 400 m flux footprint is much smaller than the footprint observed on 6/21 (Fig. 3.5a), likely due to reduced surface temperatures and convection, as seen in Fig. 3.3 and Fig. 3.4d-e. By 1700 CDT, the meteorological conditions allow for a nearly identical footprint as 1300 CDT for the MU site near the surface to produced, as can be seen in Fig 3.6d. At 400 m for this same time, the footprint has rotated to having a northeasterly source, as can be seen in Fig 3.6b. This can also be seen in the wind direction panel Fig. 3.4. This difference in source areas could be due to directional shear. Results from the radar wind profiler in the wind direction panel seem to reflect the quicker change in wind direction, compared to the surface wind direction in Fig. 3.3. Another important feature to note in the wind speed panel of Fig. 3.3-4

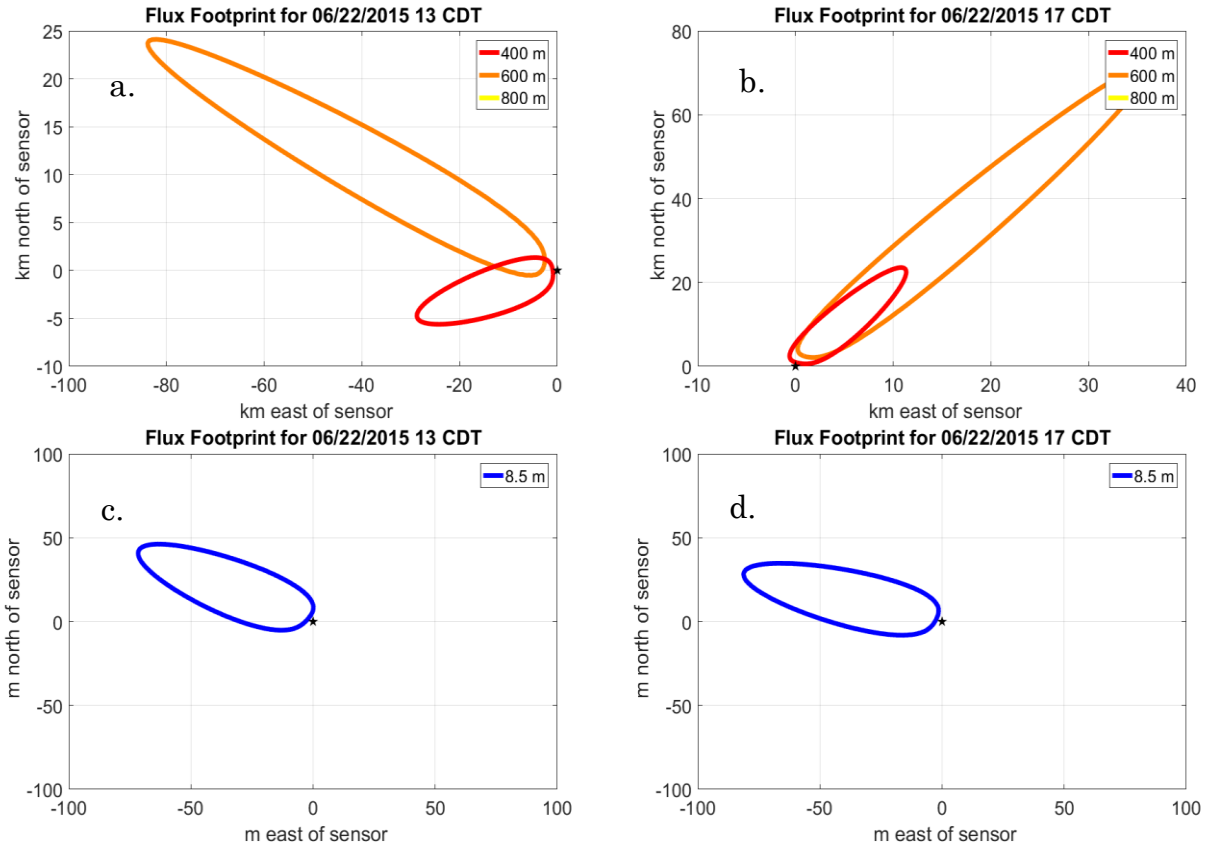

Figure 3.6. Evolution of flux footprints for 6/22/2016. Profiler footprints are shown in the top two plots, while the 8.5m footprint is shown on the bottom. Black star indicates location of sensor.

is that wind speeds close to the surface were less than 5 m/s, while wind speeds in the mid and upper portions of the boundary layer were closer to 10+ m/s. This difference may have also caused faster mixing in the upper portions of the boundary layer, while the surface layer was much slower to pick up on these changes.

The winds during the daytime on 6/23 were more homogenous than those seen on 6/21 and 6/22, with no major shifts in direction occurring. For this reason, the footprints calculated at 1300 CDT for 8.5 m, 400 m, and 600 m AGL were all aligned with a southerly wind source, as seen in Fig. 3.7. As expected, the extent of 80% of the 8.5 m footprint was in the range of 250 m, while the 400m footprint had

an upwind extent on the order of tens of kilometers, and the 600 m and 800 m footprints' extent was on the order of hundreds of km. A similar setup was seen at 1700 CDT, except the 400 m, 600 m, and 800 m footprints both had extents on the order of tens of kilometers. This may be due to the decreased wind speeds observed by the radar wind profiler at higher altitudes. This day also observed increased boundary layer heights than the day preceding it, therefore the increased vertical mixing seen may have also been why the footprints calculated above the surface were aligned with the upwind extent of the surface footprint.

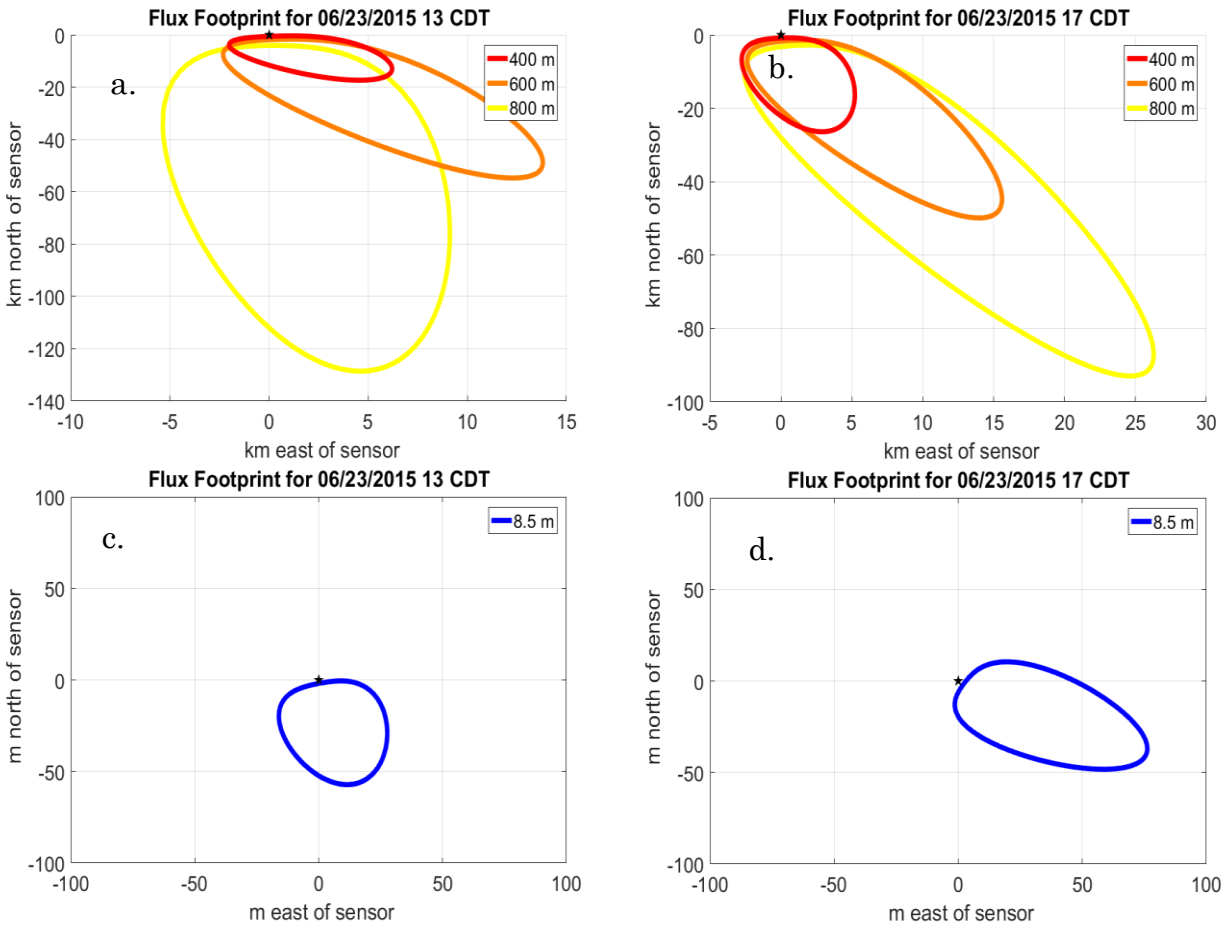

Figure 3.7. Evolution of flux footprints for 6/23/2016. Profiler footprints are shown in the top two plots, while the 8.5m footprint is shown on the bottom. Black star indicates location of sensor.

Though it would have been optimal for a flux tower to be collocated with the profiling instruments, these results show that this may have not made a major difference due to large difference in scale measured near the surface vs. in the middle and upper regions of the boundary layer. These footprint comparisons also show that in the future, it may be necessary to develop new methods to study flux in these regions of the atmosphere, as traditional techniques developed for calculating flux measurements near the surface may not suffice. However, comparisons with surface flux values still hold a lot of value, as the study of a network of surface flux

measurements within the footprint of a flux measurement made hundreds of kilometers above the surface may show a more discernable pattern. By weighting the multiple surface measurements aaccorting to the footprint weighting function, the summation of this flux would be similar to that measured at the lowest range gate of calculated water vapor fluxes.

3.3.3 Latent Heat Flux/Water Vapor Flux Divergence Within Convective Boundary Layer

For this analysis, the water vapor flux divergence was measured as the slope of the average water vapor flux profile taken between the surface and the shallowest depth of the boundary layer during the 1-hour averaging period. Since water vapor flux and latent heat flux are analogous to each other, the latent heat flux profiles are shown in order to understand the movement of energy within the boundary layer, while divergence is calculated using water vapor flux to understand how the boundary layer is evolving over time by moistening or drying. In Fig. 3.4f one can see that latent heat flux between 300 m and the boundary layer can be quite erratic and turbulent. For this reason, the flux divergence can be used as a tool to study how moisture is evolving in the boundary layer over space and time.

Additionally, the profiles of the latent heat flux are only valid within the boundary layer, in regions where optically thick clouds are not present. This is because the water vapor lidar will record erroneously high values in regions of optically thick clouds, though regions below the cloud base will still have accurate values. The radar wind profiler is also unable to accurately record winds in

turbulent-free regions above the boundary layer, due to reduced amounts of moisture and pressure gradients present, reducing Bragg scattering. Though profiles are shown above the boundary layer in this analysis, it is used as a tool to show the limits of the instruments' accuracy in calculating flux.

On 6/21, the boundary layer steadily grew during the day, reaching its maximum extent of 1.75 km at about 1700 CDT, as can be seen in Fig. 3.4. On average, negative water vapor flux divergence could be calculated from the profiles of Fig. 3.8, indicating that convergence was occurring within the column within the boundary layer. This convergence shows that moistening was occurring, as moist eddies ascended through the boundary layer, transporting moisture from the surface to higher portions of the boundary layer. This can also be seen in Fig. 3.11a, as moistening seems to occur between the hours of 13-16 CDT on 6/21. The decrease in moisture seen at 1600-1800 CDT could be attributed to the decay of the boundary layer as incoming solar radiation and convection decreases.

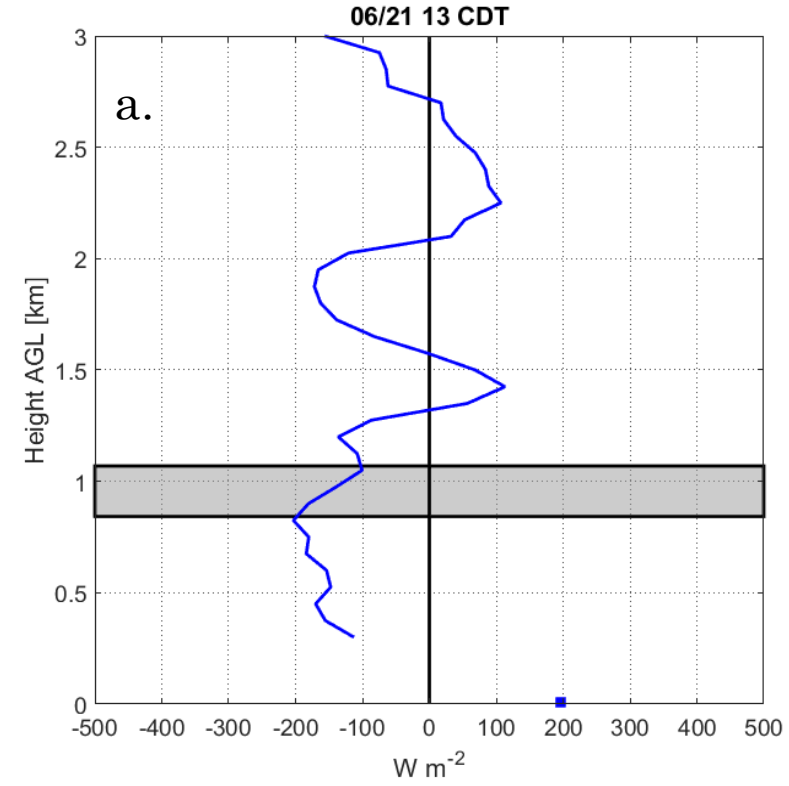
06/21 13 CDT
a.
Height AGL [km]
3
2.5
2
1.5
1
0.5
0
-500 -400 -300 -200 -100 0 100 200 300 400 500
W m-2

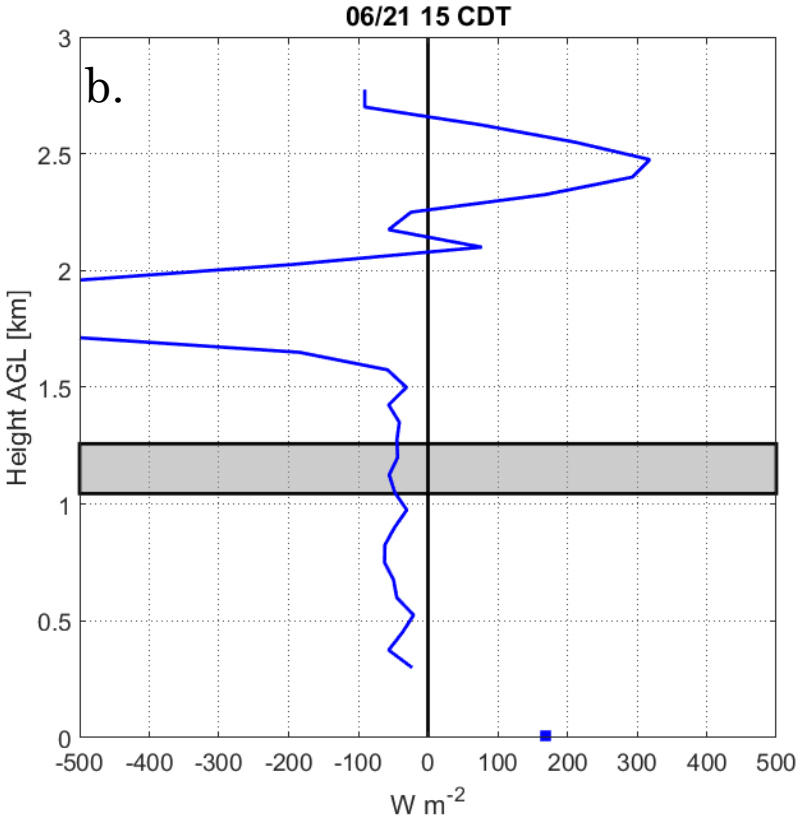
06/21 15 CDT
b.
Height AGL [km]
3
2.5
2
1.5
1
0.5
0
-500 -400 -300 -200 -100 0 100 200 300 400 500
W m-2

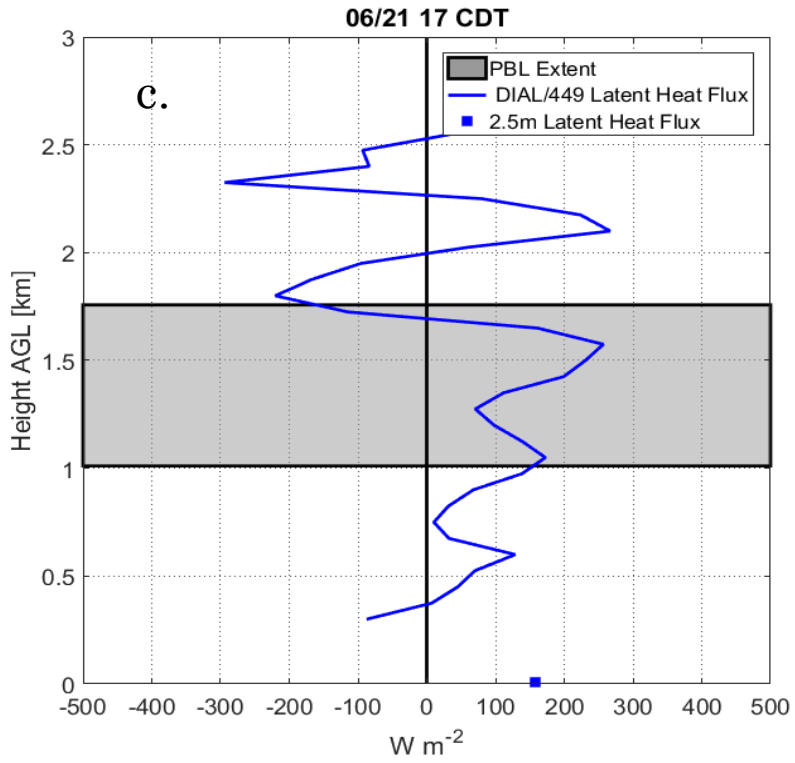

Figure 3.8. Mean profiles of latent heat flux during the afternoon of 6/21.

On 6/22, boundary layer growth was observed to stagnate to approximately 900 m from noon through about 17 CDT, as seen in Fig. 3.9. Though convergence was also calculated to occur for all three profiles on 6/22, ranging from -3.6 and 13 CDT to 5.2 g/(m^{2}s)/m at 17 CDT (Fig. 3.9c), average specific humidity values changed by less than 0.5 g/m^3, as seen at 500 m, or even decreased during the afternoon hours, as seen at the surface in Fig. 3.11b. This may have been due to more stable atmospheric conditions being present, as the strong NLLJ present the night of 6/21-6/22 would have created very stable conditions the morning of 6/22 due to a temperature inversion, thus inhibiting afternoon convection. It is interesting to note that the latent heat flux profiles within the boundary layer were positive for

nearly all profiles except for that taken at 1500 CDT (Fig. 3.9b), which could either be attributed to error, or some dry air being moved into moist air near the surface, as can be seen in Fig. 3.4a and Fig 3.3.

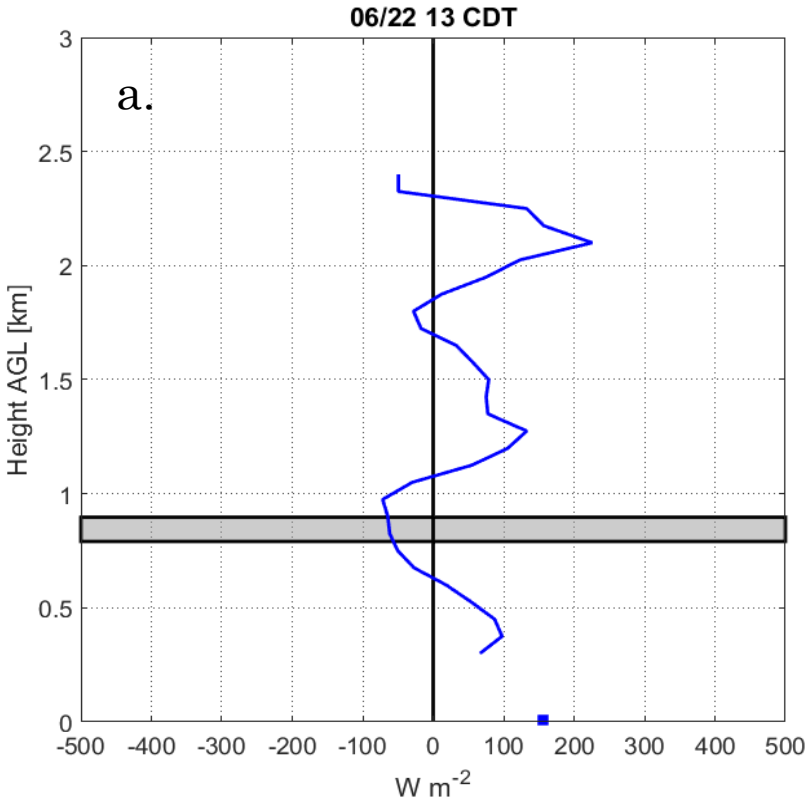
06/22 13 CDT
a.
Height AGL [km]
3
2.5
2
1.5
1
0.5
0
-500 -400 -300 -200 -100 0 100 200 300 400 500
W m-2

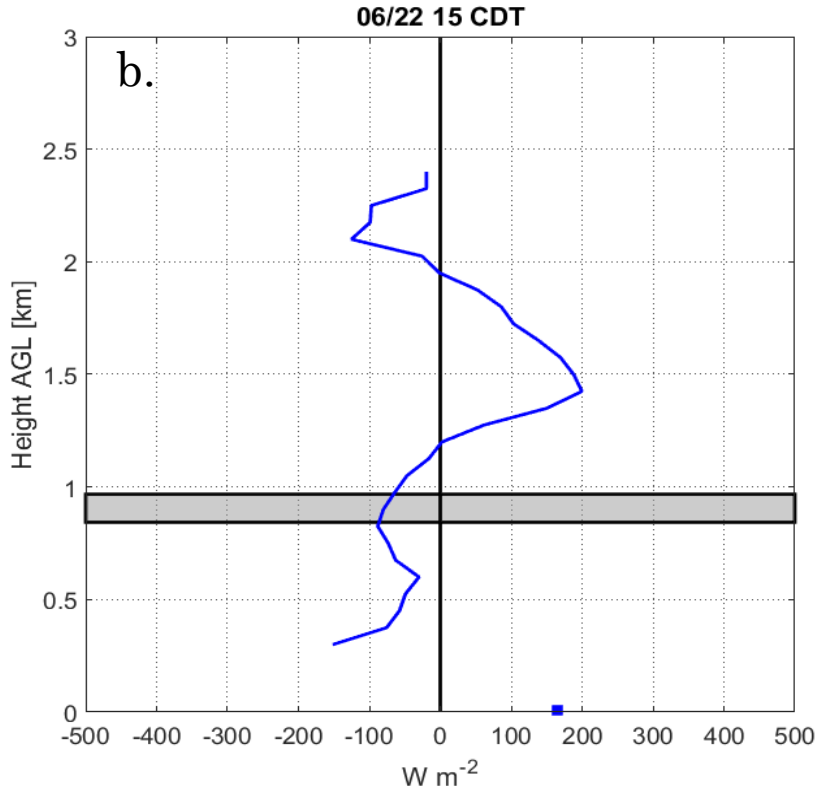
06/22 15 CDT
b.
Height AGL [km]
3
2.5
2
1.5
1
0.5
0
-500 -400 -300 -200 -100 0 100 200 300 400 500
W m-2

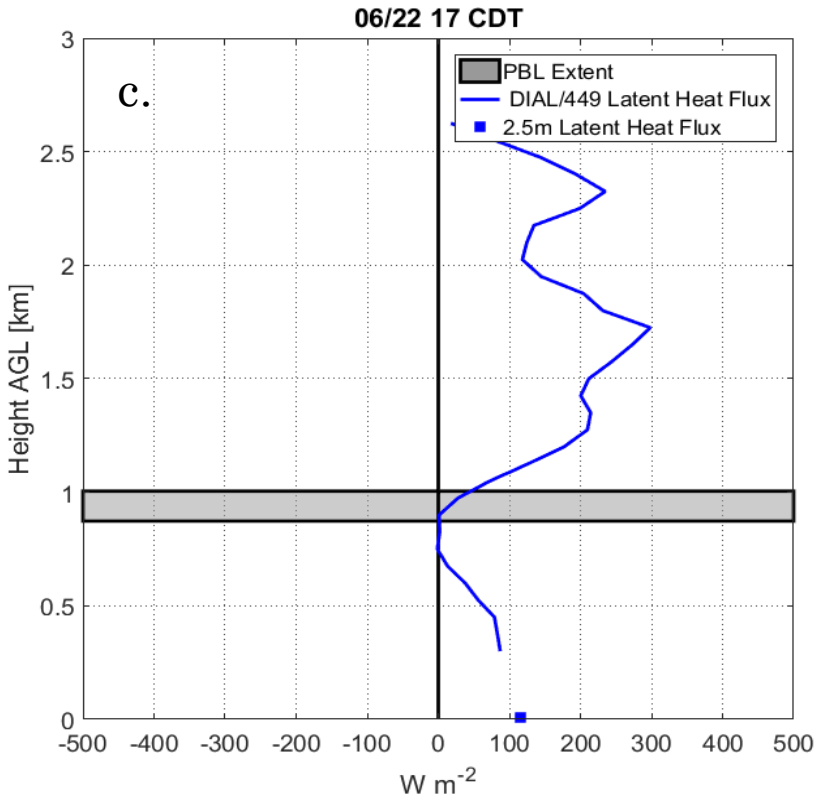

Figure 3.9. Mean profiles of latent heat flux during the afternoon of 6/22.

On 6/23, boundary layer growth increased rapidly during the afternoon under unstable, convective conditions, as can be seen in Fig. 3.4 and Fig. 3.10, reaching nearly 1.6 km AGL. Water vapor flux divergence values calculated during this time period had a much greater negative magnitude than those calculated 6/21 and 6/22 (-6.5 vs -4.3 g/(m^{2}s)/m). This can be attributed to the more unstable conditions present, as more moist parcels were able to ascend through the boundary layer and moisten this region of the atmosphere. The profiles calculated in the later afternoon have almost completely negative latent heat fluxes, which is either showing clean, dry air above the boundary layer being engulfed below, or moist air that has

ascended from the surface mixing with drier air in the entrainment layer. Dry air engulfment could also be the reason why erratic drying was observed to occur at 1000 m AGL, as seen in Fig. 3.11c.

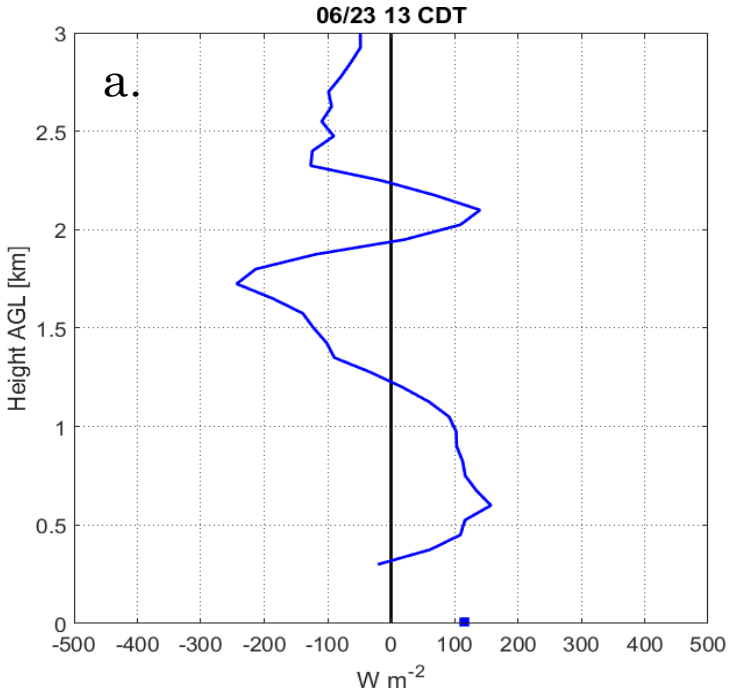

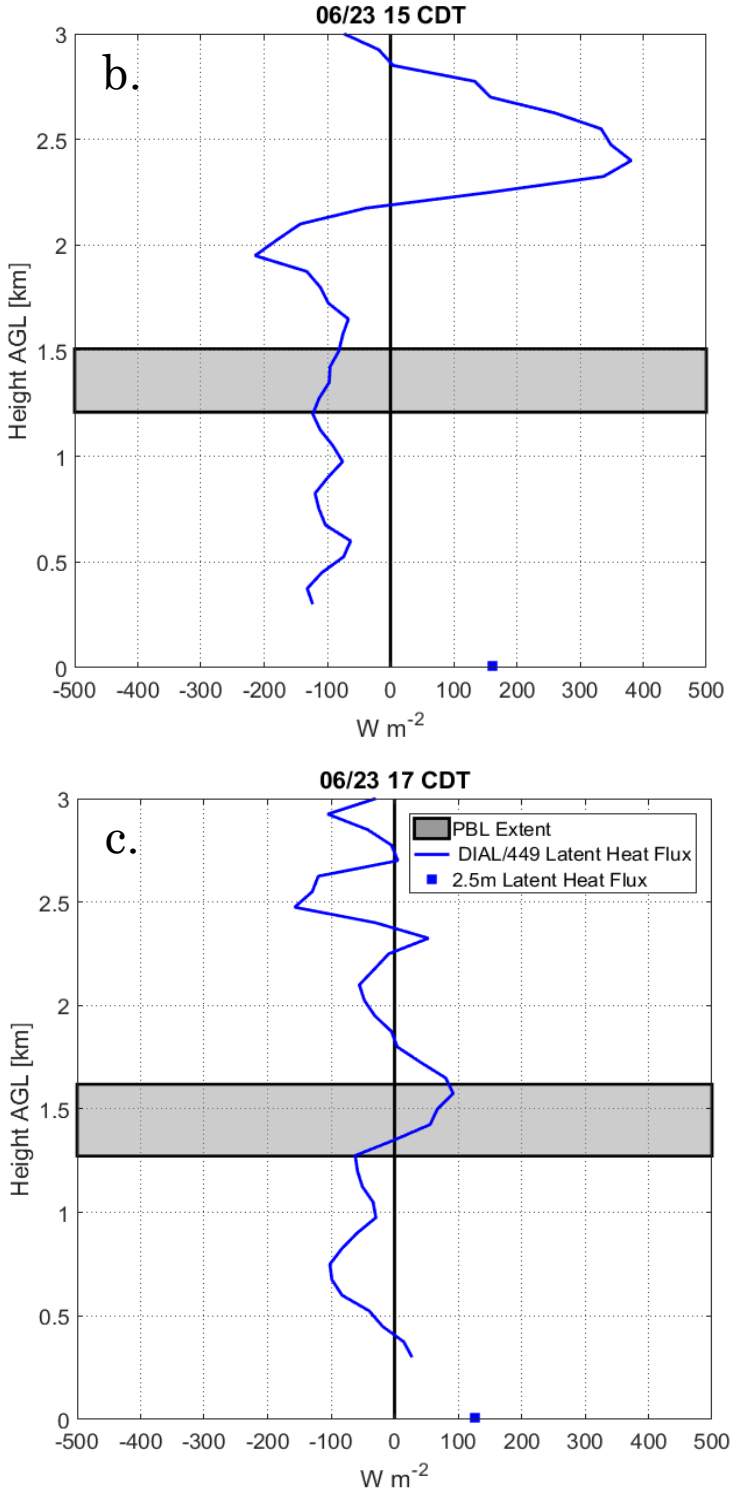

Figure 3.10. Mean profiles of latent heat flux during the afternoon of 6/23.

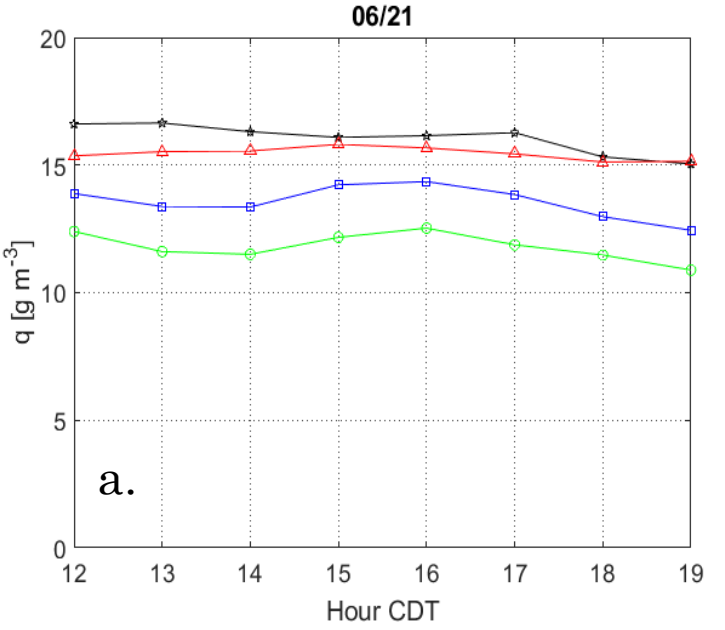
06/21
20
15
10
5
0
q [g m-3]
a.
12
13
14
15
16
17
18
19
Hour CDT

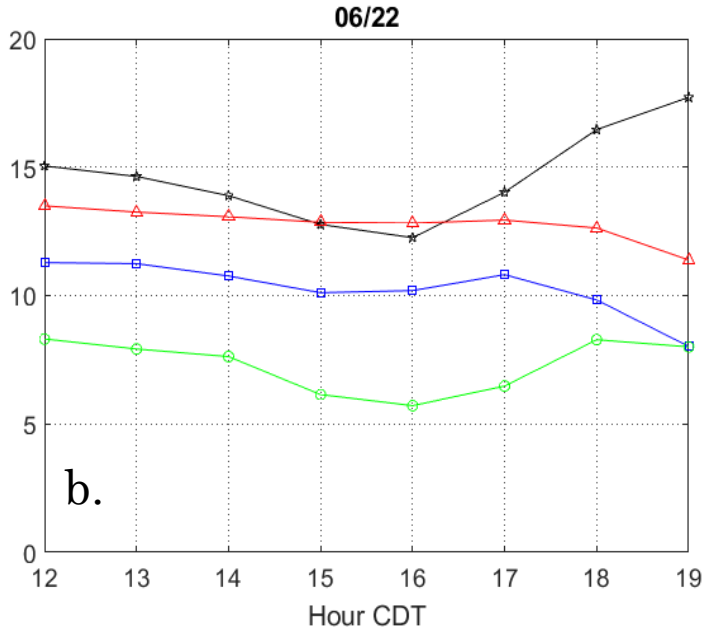
06/22
20
15
10
5
0
b.
12
13
14
15
16
17
18
19
Hour CDT

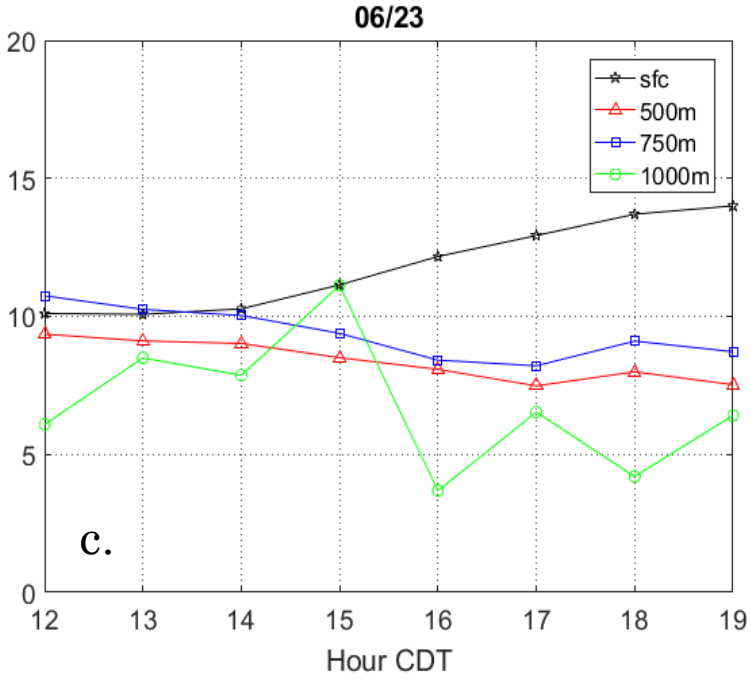

Figure 3.11. Mean specific humidity during the afternoons of a) 6/21, b) 6/22 and c) 6/23.

3.4 Conclusions

In conclusion, it has been shown that the integration of data from the water vapor DIAL and 449 MHz radar wind profile can yield interesting results when observing boundary layer processes. However, these must be taken with caution, as the DIAL experiences Mie scattering in the presence of optically think clouds, and the radar wind profiler cannot effectively use Bragg scattering to detect moisture and pressure gradients above the boundary layer. Additionally, this analysis shows that turbulence may behave differently above the surface layer, where most

traditional flux measurements and calculations have been made. In this study, this discrepancy is likely due to completely different source areas being sensed at different heights within the convective boundary layer, as the 8.5 m measurements had a source area overlapping with a small town and woody wetlands, while the measurements above 300 m had a source area comprised mainly of rural, agricultural lands. The 8.5 m measurements sense a region with roughness lengths between 0.08 - 0.7 m, while the agricultural lands, which comprise majority of the region within a 50 km radius, have roughness lengths between 0.04- 0.18 m, which shows there is significantly less surface friction over the areas being sensed above 300 m (Wieringa 1992). Therefore, the differences in land-use type as well as surface friction cause the 8.5 m and 300+ m measurements to detect entirely different sources. Locating the 8.5 m measurements in a more rural area would have been useful to partly avoid this discrepancy. It would be interesting to analyze similalr data from a larger scale study performed over homogenous land surface types, such as a large desert or large body of water.

The ability of both of these instruments to capture high frequency measurements of wind and water vapor in vertical profiles has lent itself to be extremely useful. However, future studies may benefit from higher frequency measurements, as the 30 second temporal resolution of the instrument may have left out many of the smaller turbulent eddies which may contribute a significant amount of energy to the turbulent flux measurements. An analysis which compared the difference in flux using 30 second vs. 10 second, 1 second, and higher frequency

measurements would allow for one to quantify how much of a contribution these smaller eddies make above 300 m, and whether or not the 30 second resolution of the instrument is ample for studying turbulent flux.

Footprint calculations at the different measurement heights were also able to show strong differences in source areas for flux measurements. This analysis has a tremendous impact on this study, as it shows how points that may be somewhat close in a vertical profile could be sensing moisture or any other source from areas that are entirely different topographically. In the future, it may be of good use to compare flux measurements made by these profilers with a collocated tall flux tower in order to gap the measurements that are lost within the first 300 m of the profiles. These measurements would be of great importance as they would help characterize where traditional flux calculations would be most accurate, and possibly characterize a new regime of flux calculations.

The comparison of water vapor flux divergence has also shown the value in flux measurements when averaged over longer periods, as trends in space and time become more apparent. Though the profiles of latent and water vapor flux appeared very noisy in Figs 3.8-3.10, the consistent calculation of negative water vapor flux divergence showed that convergence was occurring under the convective stable conditions, which was to be expected. Therefore, this analysis was able to show that these high frequency measurements of wind and water vapor have a lot of value in interpreting boundary layer changes in characteristics, but must be studied cautiously. Additionally, this case study serves to show a new set of tools to

interpret boundary layer dynamics, which could potentially be used to study factors that contribute to a pre-convective environment. Though this case study focused on fluxes calculated during the day, studying the late afternoon to evening transition of the turbulent flux in the convective boundary layer may be able to allow more insight into how this environment can contribute to the formation and evolution of features focused on in PECAN, such as elevated convective initiation, NLLJs, MCSs, and wave-like and bore features seen near large nocturnal convective systems at night.

3.5 Chapter Three References

Deardorff, J. W., and G. E. Willis, 1975: A parameterization of diffusion into the mixed layer. J. Appl. Meteorol., **14**, 1451–1458.

Geerts, B., and Coauthors, 2016: The 2015 Plains Elevated Convection At Night (PECAN) field project. Bull. Am. Meteorol. Soc.,.

Giez, A., G. Ehret, R. L. Schwiesow, K. J. Davis, and D. H. Lenschow, 1999: Water vapor flux measurements from ground-based vertically pointed water vapor differential absorption and Doppler lidars. J. Atmos. Ocean. Technol., **16**, 237–250.

Horst, T. W., and Jc. Weil, 1992: Footprint estimation for scalar flux measurements in the atmospheric surface layer. Boundary-Layer Meteorol., **59**, 279–296.

Kiemle, C., and Coauthors, 2007: Latent heat flux profiles from collocated airborne water vapor and wind lidars during IHOP_2002. J. Atmos. Ocean. Technol., **24**, 627–639.

Kljun, N., P. Calanca, M. W. Rotach, and H. P. Schmid, 2015: A simple two-dimensional parameterisation for Flux Footprint Prediction (FFP). Geosci. Model Dev., **8**, 3695–3713.

Kormann, R., and F. X. Meixner, 2001: An analytical footprint model for non-neutral stratification. Boundary-Layer Meteorol., **99**, 207–224.

Leclerc, M. Y., and G. W. Thurtell, 1990: Footprint prediction of scalar fluxes using a Markovian analysis. Boundary-Layer Meteorol., **52**, 247–258.

Pasquill, F., and F. B. Smith, 1983: Atmospheric diffusion.: Study of the dispersion of windborne material from industrial and other sources. JOHN WILEY SONS, 605 THIRD AVE., NEW YORK, NY 10016, USA. 1983.,.

Schmid, H. P., 1994: Source areas for scalars and scalar fluxes. Boundary-Layer Meteorol., **67**, 293–318.

——, 1997: Experimental design for flux measurements: matching scales of

observations and fluxes. Agric. For. Meteorol., **87**, 179–200.
——, and T. R. Oke, 1990: A model to estimate the source area contributing to turbulent exchange in the surface layer over patchy terrain. Q. J. R. Meteorol. Soc., **116**, 965–988.
Schuepp, P. H., M. Y. Leclerc, J. I. MacPherson, and R. L. Desjardins, 1990: Footprint prediction of scalar fluxes from analytical solutions of the diffusion equation. Boundary-Layer Meteorol., **50**, 355–373.
Stull, R. B., 1988: An introduction to boundary layer meteorology. Springer Science & Business Media,.
Turner, D. D., and U. Löhnert, 2014: Information content and uncertainties in thermodynamic profiles and liquid cloud properties retrieved from the ground-based Atmospheric Emitted Radiance Interferometer (AERI). J. Appl. Meteorol. Climatol., **53**, 752–771.
Weil, J. C., and T. W. Horst, 1992: Footprint estimates for atmospheric flux measurements in the convective boundary layer. Precip. Scav. Atmos. Exch., **2**, 717–728.
Wieringa, J., 1992: Updating the Davenport roughness classification. J. Wind Eng. Ind. Aerodyn., **41**, 357–368.

CHAPTER FOUR

Summary, Key Findings, and Conclusions

4.1 Introduction

The PECAN field campaign of 2015 was an effort to understand the nocturnal precipitation maximum in the central United States caused by the interaction between mesoscale convective systems and the stable boundary layer, nocturnal low-level jets, and atmospheric bores (Geerts et al. 2016; Turner et al. 2014). A wide array of instruments was deployed to observe these features, including a fixed site with instruments to measure surface observations and profiles of meteorological phenomena. In Ellis, Kansas, a water vapor DIAL and 449 MHz radar wind profiler were collocated and recorded measurements for the duration of the 6-week campaign form June 1st to July 16th. Another site, located 2.6 km southeast of the profilers, measured meteorological data in addition to water vapor, latent, and sensible heat flux at a height of 8.5 km. This thesis successfully developed a method to calculate water vapor flux within the convective boundary layer above 300 m, as a way to further understanding of the movement of water vapor and energy in the convective boundary layer during PECAN. Additionally, this thesis used a case study to explore how calculations derived from the latent heat and water vapor flux can yield even more information about convective

boundary layer dynamics, which can provide insight into the role of the convective boundary layer with nocturnal severe weather events.

4.2 Synthesis of Results

In conclusion, the analysis used in this thesis provided a rigorous study to characterize turbulence within the convective boundary layer over a site in Ellis, KS. A Reynolds averaging period of 90 minutes was found to be optimal for estimating flux between 300m and the height of the boundary layer. An attempt was made to characterize turbulence at night, but this proved to be more difficult due to the high altitude of the lowest range gate measured by the instruments, as well as the inability for the radar wind profiler to retrieve signal at night with minimal Bragg scattering. Further analysis also proved that rotating the three-dimensional winds in order to be orthogonal to the main flow of the wind was necessary, due to the gradually sloping topography of the prairie in central Kansas (Wilczak et al. 2001). Analysis of the integral length scale also showed a peak in λ_{max} values in regions where the boundary layer saw the most growth and decay over the shortest period of time. These λ_{max} values, on the order of hundreds of meters to the height of the boundary layer, were comparable in size seen in previous studies (Kaimal and Haugen 1969).

Further analysis of a time series of turbulent flux and meteorological data were able to reveal patterns seen under very convective, and less convective conditions over the course of three days. Water vapor and latent heat flux were compared during different times of the day through all portions of the atmosphere where a flux could be calculated. However, analysis of flux footprints revealed that the

sources of water vapor sensed near the surface could be quite different from those sensed above 300 m AGL. This analysis of meteorological data allowed for one to gain a sense of why the flux profiles calculated using the DIAL and radar wind profiler were so dramatically different from those calculated using the instruments at the 2.5m level of the MU flux tower. However, the calculation of these higher altitude flux profiles was able to reveal interesting patterns in how the profiles of flux evolve during the afternoon with the deepening of the boundary layer, and how water vapor divergence and convergence occur within a profile. The development of the tools outlined in this thesis were meant to serve as a way to gain further understanding into the development and evolution of water vapor flux profiles that has not been possible before. In the future, it is hopeful that this work can be used as a foundation for further studies, where this analysis will allow for a better understanding of boundary layer dynamics in addition to possibly gaining more insight into the turbulent mechanics of highly convective thunderstorm environments. This was especially important for the PECAN field campaign, as this work has proven to provide a new mechanism to study convective boundary layer mechanics in the environment that may precede the formation of severe, nocturnal thunderstorms, and the nocturnal, low-level jet.

4.3 Future Studies

In the future, it would be helpful to broaden the study used in this thesis in two ways. First, a network of profilers, spaced a number of kilometers apart, would be useful in studying the spatial variation of turbulence, both vertically and

horizontally. Additionally, these measurements would also allow for advection of latent heat and water vapor to be studied, which was not possible for the analysis used in this thesis. Second, co-locating a DIAL and wind profiler with a tall tower would be extremely useful to bridge the gap between surface and mid-tropospheric turbulence studies. It would also be interesting to study water vapor and latent heat flux profiles on days where convection occurred later in the afternoon, or on days where convection occurred at night, in order to see if any significant patterns could be discernable from the six weeks of data available. From a very limited preliminary analysis using t-tests between different profiles of water vapor, there was some significance seen in the profiles on days where convection did and did not occur, with days with higher amounts of water vapor having a higher probability of convection occurring. Though nighttime profiles of water vapor did not show any significant differences between nights that did and did not have convection, a more rigorous analysis would be needed to prove this.

Additionally, future studies would benefit from using water vapor and wind profilers with similar optical sensing methods. For this study, a water vapor lidar, which cannot see through optically thick clouds, and a radar wind profiler, which cannot effectively scatter in low turbulence conditions, were used together to calculate profiles of water vapor and latent heat flux. Because of this, using the instruments together caused for more limited conditions for data to be taken, unlike if similar optical measuring methods had been used. For example, if a wind lidar had been used with the DIAL, nighttime turbulence measurements may have been

possible to study. An analogous water vapor instrument to the 449 MHz wind profiler is not available, but this would allow for measurements of water vapor and latent heat flux within a cloud to be possible. However, the synergy of the DIAL and 449 MHz wind profiler for the duration of the PECAN field campaign were still able to show great potential for calculating water vapor flux profiles.

4.4 Comprehensive References

Angevine, W. M., A. B. White, and S. K. Avery, 1994: Boundary-layer depth and entrainment zone characterization with a boundary-layer profiler. Boundary-Layer Meteorol., **68**, 375–385.

Aubinet, M., B. Heinesch, and B. Longdoz, 2002: Estimation of the carbon sequestration by a heterogeneous forest: Night flux corrections, heterogeneity of the site and inter-annual variability. Glob. Chang. Biol., **8**, 1053–1071.

Bakwin, P. S., P. P. Tans, D. F. Hurst, and C. Zhao, 1998: Measurements of carbon dioxide on very tall towers: results of the NOAA/CMDL program. Tellus B, **50**, 401–415.

Baldocchi, D., E. Falge, L. Gu, R. Olson, and others, 2001: FLUXNET: A new tool to study the temporal and spatial variability of ecosystem-scale carbon dioxide, water vapor, and energy flux densities. Bull. Am. Meteorol. Soc., **82**, 2415.

Berger, B. W., K. J. Davis, C. Yi, P. S. Bakwin, and C. L. Zhao, 2001: Long-term carbon dioxide fluxes from a very tall tower in a northern forest: flux measurement methodology. J. Atmos. Ocean. Technol., **18**, 529–542.

Blanken, P. D., 1998: Turbulent Flux Measurements Above and Below the Overstory of a Boreal Aspen Forest. Boundary-Layer Meteorol., **89**, 109–140, doi:10.1023/A:1001557022310. http://dx.doi.org/10.1023/A:1001557022310.

Briggs, B. H., G. J. Phillips, and D. H. Shinn, 1950: The analysis of observations on spaced receivers of the fading of radio signals. Proc. Phys. Soc. Sect. B, **63**, 106.

Cohn, S. A., C. L. Holloway, S. P. Oncley, R. J. Doviak, and R. J. Lataitis, 1997: Validation of a UHF spaced antenna wind profiler for high-resolution boundary layer observations. Radio Sci., **32**, 1279–1296.

Davis, K. J., P. S. Bakwin, C. Yi, B. W. Berger, C. Zhao, R. M. Teclaw, and J. G. Isebrands, 2003: The annual cycles of CO2 and H2O exchange over a northern mixed forest as observed from a very tall tower. Glob. Chang. Biol., **9**, 1278–1293.

Deacon, E. L., and E. B. Kraus, 1968: The levelling error in Reynolds stress measurement. Bull. Am. Meteorol. Soc, **49**, 836.

Deardorff, J. W., and G. E. Willis, 1975: A parameterization of diffusion into the mixed layer. J. Appl. Meteorol., **14**, 1451–1458.

Desai, A. R., and Coauthors, 2015: Landscape-level terrestrial methane flux

observed from a very tall tower. Agric. For. Meteorol., **201**, 61–75.
Desjardins, R. L., J. I. MacPherson, P. H. Schuepp, and F. Karanja, 1989: An evaluation of aircraft flux measurements of CO2, water vapor and sensible heat. Boundary Layer Studies and Applications, Springer, 55–69.
Dyer, A. J., 1981: Flow distortion by supporting structures. Boundary-Layer Meteorol., **20**, 243–251.
Ecklund, W. L., D. A. Carter, and B. B. Balsley, 1988: A UHF wind profiler for the boundary layer: Brief description and initial results. J. Atmos. Ocean. Technol., **5**, 432–441.
Ehret, G., K. P. Hoinka, J. Stein, A. Fix, C. Kiemle, and G. Poberaj, 1999: Low stratospheric water vapor measured by an airborne DIAL. J. Geophys. Res. Atmos., **104**, 31351–31359.
Foken, T., and C. J. Nappo, 2008: Micrometeorology. Springer Science & Business Media,.
Geerts, B., and Coauthors, 2016: The 2015 Plains Elevated Convection At Night (PECAN) field project. Bull. Am. Meteorol. Soc.,.
Giez, A., G. Ehret, R. L. Schwiesow, K. J. Davis, and D. H. Lenschow, 1999: Water vapor flux measurements from ground-based vertically pointed water vapor differential absorption and Doppler lidars. J. Atmos. Ocean. Technol., **16**, 237–250.
Horst, T. W., and Jc. Weil, 1992: Footprint estimation for scalar flux measurements in the atmospheric surface layer. Boundary-Layer Meteorol., **59**, 279–296.
Kaimal, J. C., and D. A. Haugen, 1969: Some errors in the measurement of Reynolds stress. J. Appl. Meteorol., **8**, 460–462.
Kaimal, J. C., and J. J. Finnigan, 1994: Atmospheric boundary layer flows: their structure and measurement. Oxford University Press,.
Kiemle, C., G. Ehret, A. Giez, K. J. Davis, D. H. Lenschow, and S. P. Oncley, 1997: Estimation of boundary layer humidity fluxes and statistics from airborne differential absorption lidar (DIAL). J. Geophys. Res. Atmos., **102**, 29189–29203.
——, and Coauthors, 2007: Latent heat flux profiles from collocated airborne water vapor and wind lidars during IHOP_2002. J. Atmos. Ocean. Technol., **24**, 627–639.
Kljun, N., P. Calanca, M. W. Rotach, and H. P. Schmid, 2015: A simple two-dimensional parameterisation for Flux Footprint Prediction (FFP). Geosci. Model Dev., **8**, 3695–3713.
Kolmogorov, A. N., 1941a: Dissipation of energy in locally isotropic turbulence. Dokl. Akad. Nauk SSSR, Vol. 32 of, 16–18.
Kolmogorov, A. N., 1941b: The local structure of turbulence in incompressible viscous fluid for very large Reynolds numbers. Dokl. Akad. Nauk SSSR, Vol. 30 of, 301–305.
Kormann, R., and F. X. Meixner, 2001: An analytical footprint model for non-neutral stratification. Boundary-Layer Meteorol., **99**, 207–224.
Leclerc, M. Y., and G. W. Thurtell, 1990: Footprint prediction of scalar fluxes using

a Markovian analysis. Boundary-Layer Meteorol., **52**, 247–258.
Lee, X., W. Massman, and B. Law, 2006: Handbook of micrometeorology: a guide for surface flux measurement and analysis. Springer Science & Business Media,.
Lindseth, B., W. O. J. Brown, J. Jordan, D. Law, T. Hock, S. A. Cohn, and Z. Popovic, 2012a: A New Portable 449-MHz Spaced Antenna Wind Profiler Radar. IEEE Trans. Geosci. Remote Sens., **50**, 3544–3553.
——, T. Kelly, W. O. J. Brown, T. Hock, S. A. Cohn, and Z. Popovic, 2012b: Low-cost 63% efficient 2.5-kW UHF power amplifier for a wind profiler radar. Microwave Symposium Digest (MTT), 2012 IEEE MTT-S International, 1–3.
——, W. O. J. Brown, T. Hock, S. A. Cohn, and Z. Popović, 2014: Wind profiler radar antenna sidelobe reduction. IEEE Trans. Antennas Propag., **62**, 56–63.
Linné, H., B. Hennemuth, J. Bösenberg, and K. Ertel, 2007: Water vapour flux profiles in the convective boundary layer. Theor. Appl. Climatol., **87**, 201–211.
Pasquill, F., and F. B. Smith, 1983: Atmospheric diffusion.: Study of the dispersion of windborne material from industrial and other sources. JOHN WILEY SONS, 605 THIRD AVE., NEW YORK, NY 10016, USA. 1983.,.
Schmid, H. P., 1994: Source areas for scalars and scalar fluxes. Boundary-Layer Meteorol., **67**, 293–318.
——, 1997: Experimental design for flux measurements: matching scales of observations and fluxes. Agric. For. Meteorol., **87**, 179–200.
——, and T. R. Oke, 1990: A model to estimate the source area contributing to turbulent exchange in the surface layer over patchy terrain. Q. J. R. Meteorol. Soc., **116**, 965–988.
Schuepp, P. H., M. Y. Leclerc, J. I. MacPherson, and R. L. Desjardins, 1990: Footprint prediction of scalar fluxes from analytical solutions of the diffusion equation. Boundary-Layer Meteorol., **50**, 355–373.
Senff, C., J. Bösenberg, and G. Peters, 1994: Measurement of water vapor flux profiles in the convective boundary layer with lidar and radar-RASS. J. Atmos. Ocean. Technol., **11**, 85–93.
Spuler, S. M., K. S. Repasky, B. Morley, D. Moen, M. Hayman, and A. R. Nehrir, 2014: Field deployable diode-laser-based differential absorption lidar (DIAL) for profiling water vapor. Atmos. Meas. Tech. Discuss., **7**, 11265–11302.
——, ——, ——, ——, ——, and ——, 2015: Field-deployable diode-laser-based differential absorption lidar (DIAL) for profiling water vapor. Atmos. Meas. Tech., **8**, 1073–1087.
Stull, R. B., 1988: An introduction to boundary layer meteorology. Springer Science & Business Media,.
Taylor, G. I., 1938: The spectrum of turbulence. Proceedings of the Royal Society of London A: Mathematical, Physical and Engineering Sciences, Vol. 164 of, 476–490.
Turner, D., D. Parsons, and B. Geerts, 2014: Plains Elevated Convection at Night (PECAN) Experiment Science Plan.
Turner, D. D., and U. Löhnert, 2014: Information content and uncertainties in thermodynamic profiles and liquid cloud properties retrieved from the ground-

based Atmospheric Emitted Radiance Interferometer (AERI). J. Appl. Meteorol. Climatol., **53**, 752–771.

——, J. E. M. Goldsmith, and R. A. Ferrare, EJ Mlawer, and HE Revercomb, 2016: Water vapor observations in the ARM Program. Atmos. Radiat. Meas. Progr. First 20 Years, Meteor. Monogr,.

USDA, 2015: USDA National Agricultural Statistics Service Cropland Data Layer. Washington, D.C.,.

Weckwerth, T. M., K. J. Weber, D. D. Turner, and S. M. Spuler, 2016: Validation of a Water Vapor Micropulse Differential Absorption Lidar (DIAL). J. Atmos. Ocean. Technol., **33**, 2353–2372.

Weil, J. C., and T. W. Horst, 1992: Footprint estimates for atmospheric flux measurements in the convective boundary layer. Precip. Scav. Atmos. Exch., **2**, 717–728.

Wieringa, J., 1992: Updating the Davenport roughness classification. J. Wind Eng. Ind. Aerodyn., **41**, 357–368.

Wilczak, J. M., S. P. Oncley, and S. A. Stage, 2001: Sonic anemometer tilt correction algorithms. Boundary-Layer Meteorol., **99**, 127–150.

Willis, G. E., and J. W. Deardorff, 1976: On the use of Taylor's translation hypothesis for diffusion in the mixed layer. Q. J. R. Meteorol. Soc., **102**, 817–822.

Wulfmeyer, V., 1999: Investigation of turbulent processes in the lower troposphere with water vapor DIAL and radar-RASS. J. Atmos. Sci., **56**, 1055–1076.

Wulfmeyer, V., and Coauthors, 2015: A review of the remote sensing of lower tropospheric thermodynamic profiles and its indispensable role for the understanding and the simulation of water and energy cycles. Rev. Geophys., **53**, 819–895.

——, S. K. Muppa, A. Behrendt, E. Hammann, F. Späth, Z. Sorbjan, D. D. Turner, and R. M. Hardesty, 2016: Determination of convective boundary layer entrainment fluxes, dissipation rates, and the molecular destruction of variances: theoretical description and a strategy for its confirmation with a novel lidar system synergy. J. Atmos. Sci., **73**, 667–692.

2012: User's Guide: VAISALA Weather Transmitter WXT-520. Helsinki, 171 pp. http://www.vaisala.com/Vaisala Documents/User Guides and Quick Ref Guides/M210906EN-C.pdf.